

1 **Aging impairs cold-induced beige adipogenesis and adipocyte metabolic reprogramming**

2

3 Corey D. Holman^{1,2}, Alexander P. Sakers^{1,2}, Ryan P. Calhoun^{1,2}, Lan Cheng^{1,2}, Ethan C. Fein^{1,2},

4 Christopher Jacobs^{3,4}, Linus Tsai,³⁻⁵ Evan D. Rosen,³⁻⁵ and Patrick Seale^{1,2,*}

5

6 1. Institute for Diabetes, Obesity & Metabolism; Perelman School of
7 Medicine at the University of Pennsylvania, Philadelphia, PA, USA

8 2. Department of Cell and Developmental Biology; Perelman School of
9 Medicine at the University of Pennsylvania, Philadelphia, PA, USA

10 3. Division of Endocrinology, Diabetes, and Metabolism, Beth Israel
11 Deaconess Medical Center, Boston, MA, USA

12 4. Broad Institute of MIT and Harvard, Cambridge, MA, USA

13 5. Harvard Medical School, Boston, MA, USA

14

15 *Correspondence should be addressed to:

16 Patrick Seale

17 Perelman School of Medicine

18 University of Pennsylvania

19 Smilow Center for Translational Research

20 3400 Civic Center Blvd, Rm. 12-105

21 Philadelphia, PA, 19104. USA

22 Tel: 215-573-8856

23 Email: sealep@pennmedicine.upenn.edu

24 **Abstract**

25 The energy-burning capability of beige adipose tissue is a potential therapeutic tool for
26 reducing obesity and metabolic disease, but this capacity is decreased by aging. Here, we
27 evaluate the impact of aging on the profile and activity of adipocyte stem and progenitor cells
28 (ASPCs) and adipocytes during the beiging process. We found that aging increases the
29 expression of *Cd9* and other fibrogenic genes in fibroblastic ASPCs and blocks their differentiation
30 into beige adipocytes. Fibroblastic ASPC populations from young and aged mice were equally
31 competent for beige differentiation *in vitro*, suggesting that environmental factors suppress
32 adipogenesis *in vivo*. Examination of adipocytes by single nucleus RNA-sequencing identified
33 compositional and transcriptional differences in adipocyte populations with age and cold
34 exposure. Notably, cold exposure induced an adipocyte population expressing high levels of *de*
35 *novo* lipogenesis (DNL) genes, and this response was severely blunted in aged animals. We
36 further identified natriuretic peptide clearance receptor *Npr3*, a beige fat repressor, as a marker
37 gene for a subset of white adipocytes and an aging-upregulated gene in adipocytes. In summary,
38 this study indicates that aging blocks beige adipogenesis and dysregulates adipocyte responses
39 to cold exposure and provides a unique resource for identifying cold and/or aging-regulated
40 pathways in adipose tissue.

41 Introduction

42 Brown and beige fat cells are specialized to burn calories for heat production in response
43 to certain stimuli and have the capacity to reduce obesity and metabolic disease. Brown
44 adipocytes are localized in dedicated brown adipose tissue (BAT) depots, whereas beige
45 adipocytes develop in white adipose tissue (WAT) in response to cold exposure, and other stimuli
46 (W. Wang & Seale, 2016). Adult humans possess thermogenic adipose depots that resemble
47 rodent beige adipose tissue (Jespersen et al., 2013; Wu et al., 2012). Brown and beige adipocytes
48 share similar cellular features such as abundant mitochondria, multilocular lipid droplets, and
49 expression of thermogenic genes like Uncoupling Protein-1 (UCP1). UCP1, when activated,
50 dissipates the mitochondrial proton gradient, leading to high levels of substrate oxidation and heat
51 production (Cannon & Nedergaard, 2004). Brown and beige adipocytes can also produce heat
52 via several other UCP1-independent futile cycles (Chouchani, Kazak, & Spiegelman, 2019).

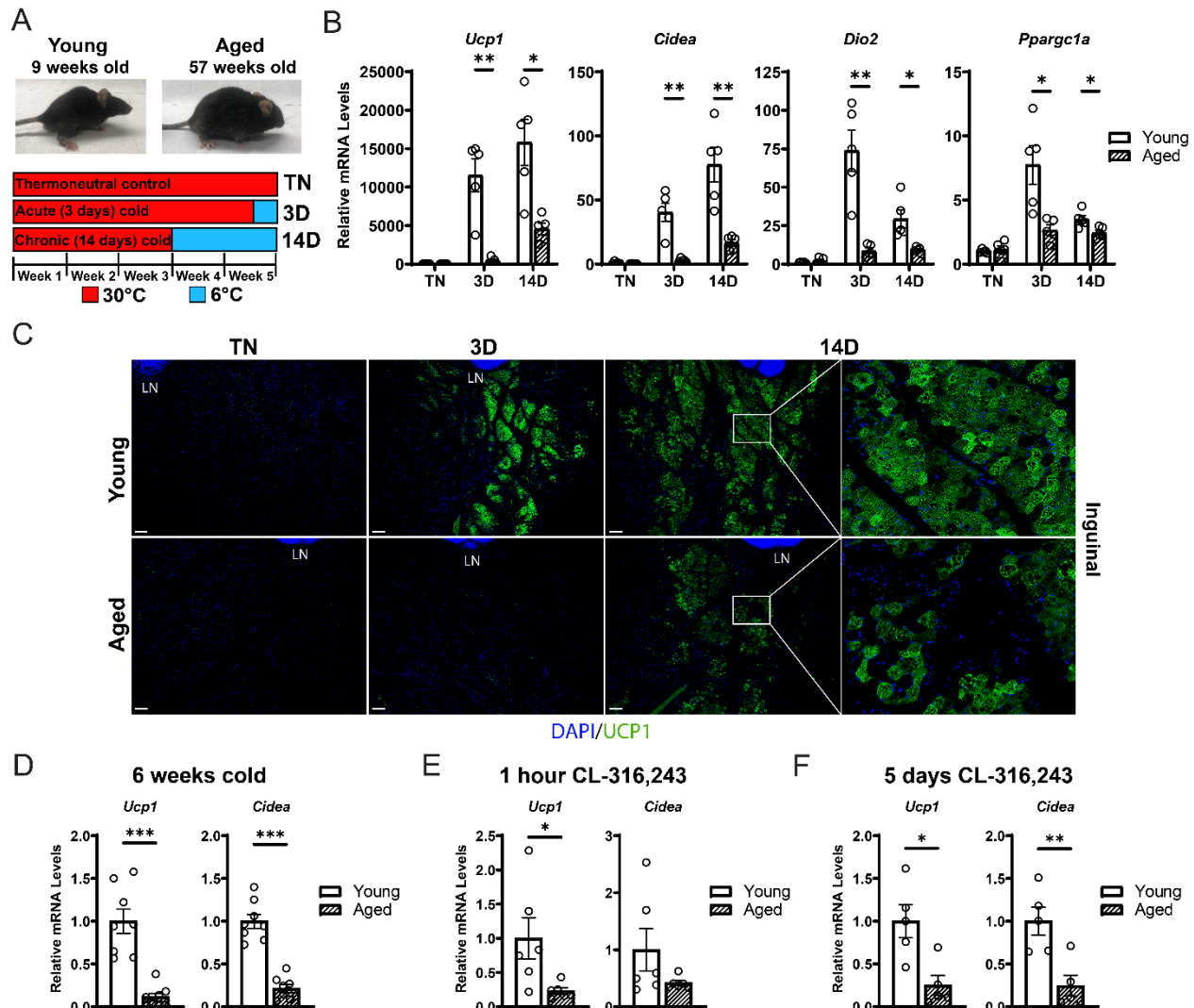
53 Increasing beige fat development in mice reduces obesity and improves insulin sensitivity,
54 whereas ablation of beige fat in mice causes metabolic dysfunction (Cederberg et al., 2001;
55 Cohen et al., 2014; Seale et al., 2011; Shao et al., 2016; Stine et al., 2016). Furthermore,
56 transplantation of human beige adipocytes into obese mice reduces liver steatosis and improves
57 metabolic health (Min et al 2016). Beige adipocytes develop via the *de novo* differentiation of
58 adipocyte precursor cells (ASPCs) or through induction of the thermogenic program in adipocytes
59 (Ferrero, Rainer, & Deplancke, 2020; Sakers, De Siqueira, Seale, & Villanueva, 2022; Shao et
60 al., 2019).

61 Human and mouse thermogenic adipose tissue activity declines with aging, predisposing
62 to cardiometabolic disease and limiting the potential of brown/beige fat targeted therapies (Becher
63 et al., 2021; Berry et al., 2017; Cypess et al., 2012; Rogers, Landa, Park, & Smith, 2012; W. Wang
64 et al., 2019; Yoneshiro et al., 2011). In mice, beige adipose tissue is reduced by 'middle-age' (i.e.,
65 1-year-old), preceding many of the damaging effects of old age on organ function (Berry et al.,
66 2017; Goncalves et al., 2017; Rogers et al., 2012). The aging-associated decline in beige fat
67 activity can occur independently of increases in body weight (Rogers et al., 2012; St-Onge, 2005).
68 A variety of processes and pathways have been linked to the aging-induced deficit in beige fat
69 formation, including diminished proliferation and cellular senescence of ASPCs (Berry et al.,
70 2017), increased fibrosis (W. Wang et al., 2019), increased inflammation (Amiya Kumar Ghosh,
71 2019), accumulation of anti-adipogenic regulatory cells (Nguyen et al., 2021), and reduced
72 adrenergic tone (Rogers et al., 2012). However, a detailed understanding of how cold exposure
73 and aging affect ASPC identity, adipogenesis, and adipocyte phenotypic switching remains
74 elusive.

75 We applied ASPC lineage tracing, along with unbiased single-cell and single-nucleus RNA
76 sequencing (scRNA-seq; snRNA-seq) to comprehensively profile the beiging process and
77 evaluated the impact of aging on this process. We found that aging modulates the gene program
78 of multiple fibroblastic ASPC populations and blocks the differentiation of these cells into beige
79 adipocytes *in vivo*. snRNA-seq analysis revealed four types of adipocytes defined by different
80 responses to cold exposure and aging: beige, *Npr3*-high, *de novo* lipogenesis (DNL)-low, and
81 DNL-high. Notably, DNL-high adipocytes were defined by the marked induction of DNL genes
82 during cold exposure in young compared to aged animals. A white adipocyte subpopulation in
83 young mice were marked by expression of Natriuretic peptide receptor-3 (*Npr3*), which was also
84 increased in multiple adipocyte populations of aged mice. Altogether, this study shows that aging
85 blocks cold-stimulated adipocyte reprogramming and ASPC adipogenesis and implicates
86 suppression of natriuretic peptide signaling and DNL in contributing to the aging-mediated decline
87 in beige fat formation.

88 **Results**

Figure 1



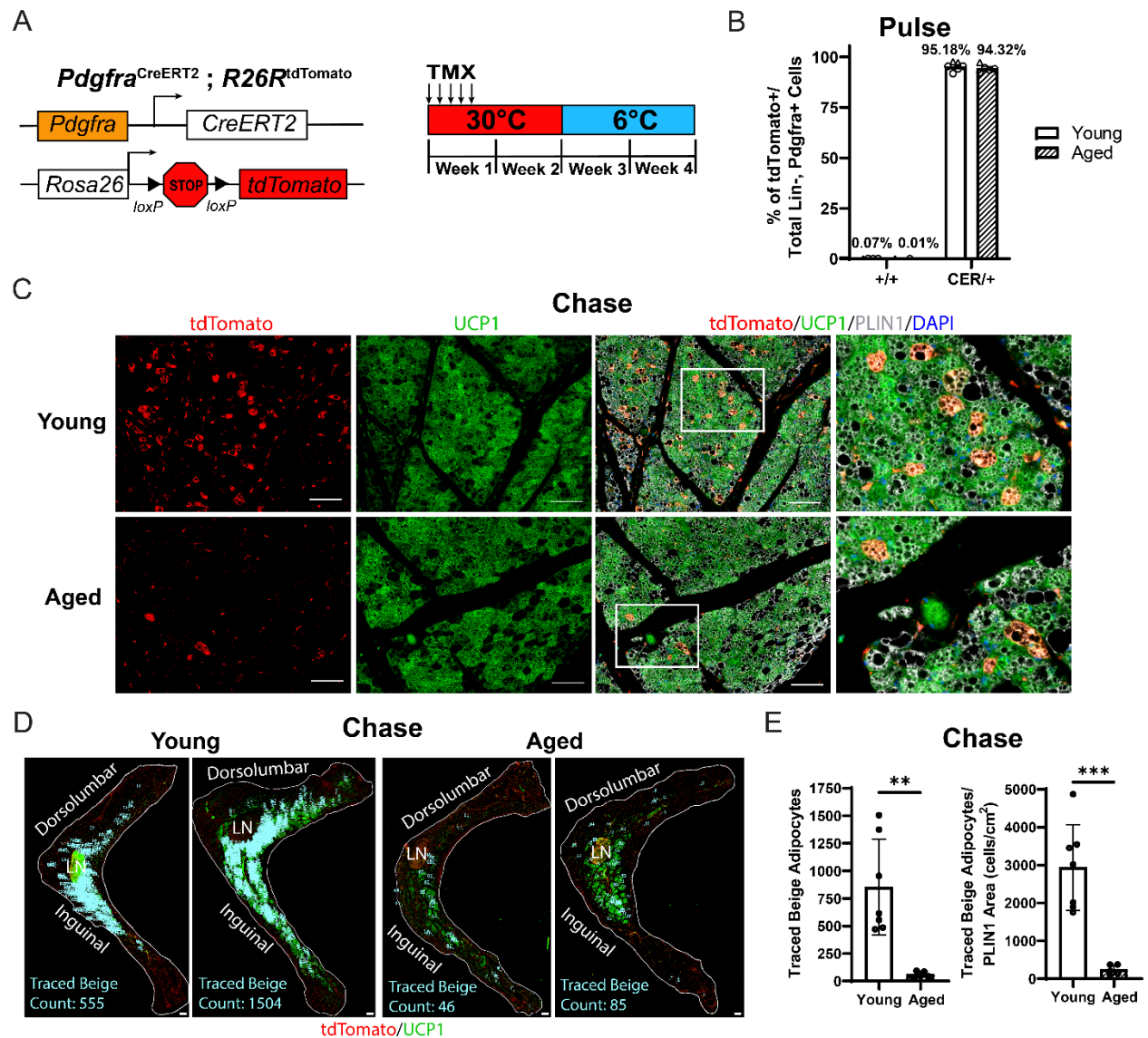
89 **Figure 1. Aged mice exhibit decreased iWAT beiging in response to cold exposure or β 3-agonist treatment.** (A) Young
 90 (9-week-old) and aged (57-week-old) C57BL/6 mice were acclimated to 30°C for 3 weeks, followed by two additional weeks
 92 remaining at 30°C (TN, thermoneutral controls), spending the last 3 days at 6°C (3D, acute cold) or last 14 days at 6°C (14D,
 93 chronic cold). (B) Relative mRNA levels of thermogenic marker genes in mouse iWAT from (A), n=5. (C) Immunofluorescence
 94 analysis of UCP1 (green) and DAPI (blue) in iWAT sections from mice in (A), LN = lymph node. Scale bar 100 μ m. (D-F)
 95 Relative mRNA levels of *Ucp1* and *Cidea* in iWAT from young and aged mice that were either: exposed to 6°C cold for 6
 96 weeks (D), treated with CL-316,243 for 1 hour (E) or treated with CL 316,243 for 5 days (F). Data represent mean \pm SEM,
 97 points represent biological replicates, 2 groups analyzed using a Student's t-test, and multiple conditions analyzed with a
 98 Holm-Šidák correction for multiple comparisons. Significance: not significant, $P > 0.05$; * $P < 0.05$ ** $P < 0.01$; *** $P < 0.001$.

99 **Aging impairs iWAT beiging**

100 To study the impact of aging on beige adipose tissue development, we exposed young (9-
101 week-old) and middle aged (57-week-old) C57BL/6 mice to 6°C for either 3 or 14 days. All mouse
102 groups were first acclimated to 30°C (thermoneutrality [TN]) for 3 weeks to reduce beige adipose
103 tissue to baseline (low) levels. Following acclimation, TN-housed mice remained at 30°C; acute
104 cold mice (3D) were transitioned to 6°C after 11 days for the final 3 days; and chronic cold mice
105 (14D) were moved to 6°C for two weeks (**Figure 1A**). As expected, the aged mice weighed more
106 and had larger iWAT depots than the young mice (**Figure S1A,B**). Cold exposure greatly and
107 progressively increased the expression levels of thermogenic genes *Ucp1*, *Cidea*, *Dio2* and
108 *Ppargc1a* in young iWAT, but the activation of these genes was significantly blunted in aged mice,
109 especially at the 3D timepoint (**Figure 1B**). Immunofluorescence staining showed a robust
110 induction of UCP1 protein in multilocular adipocytes of young iWAT at 3D of cold exposure, which
111 was further increased at 14D. The induction of UCP1⁺ beige adipocytes was severely reduced in
112 aged animals, with strikingly few UCP1⁺ adipocytes detected at. At 14D, the beige adipocytes in
113 young and aged look morphologically similar, although there are fewer in aged. (**Figure 1C**).
114 Beige adipocytes in young and aged were most prominent in the inguinal region (versus
115 dorsolumbar) of iWAT, consistent with other reports (Barreau et al., 2016; Chi et al., 2018;
116 Dichamp et al., 2019) and beiging was largely absent in the dorsolumbar region of aged mice
117 (**Figure S1C-D**). To determine if the beiging response is delayed in aged mice, we exposed young
118 and aged mice at 6°C for 6 weeks. At this time point, the iWAT of aged mice exhibited a larger
119 deficit in thermogenic gene expression compared to young animals (**Figure 1D**). Thermogenic
120 gene levels in interscapular BAT were similar between young and aged mice, at TN and after cold
121 exposure, indicating that the inhibitory effects of aging were selective to WAT (**Figure S1E**).

122 Next, we examined beige fat formation in young and aged animals upon treatment with
123 the β 3-selective adrenergic agonist CL-316,243 (CL). CL acts in an adipose tissue autonomous
124 manner to stimulate beige fat biogenesis, bypassing the central nervous system pathways that
125 mediate the response to cold exposure. Acute CL treatment for only 1 hour increased iWAT *Ucp1*
126 expression in young mice to a much greater extent than in aged mice (**Figure 1E**). Chronic CL
127 exposure for 5 days also induced much higher expression levels of *Ucp1* and *Cidea* in iWAT of
128 young compared to aged mice (**Figure 1F**). Taken together, these results demonstrate that beige
129 adipose tissue induction is severely impaired in middle aged mice.

Figure 2



130
131
132
133
134
135
136
137
138
139
140
141

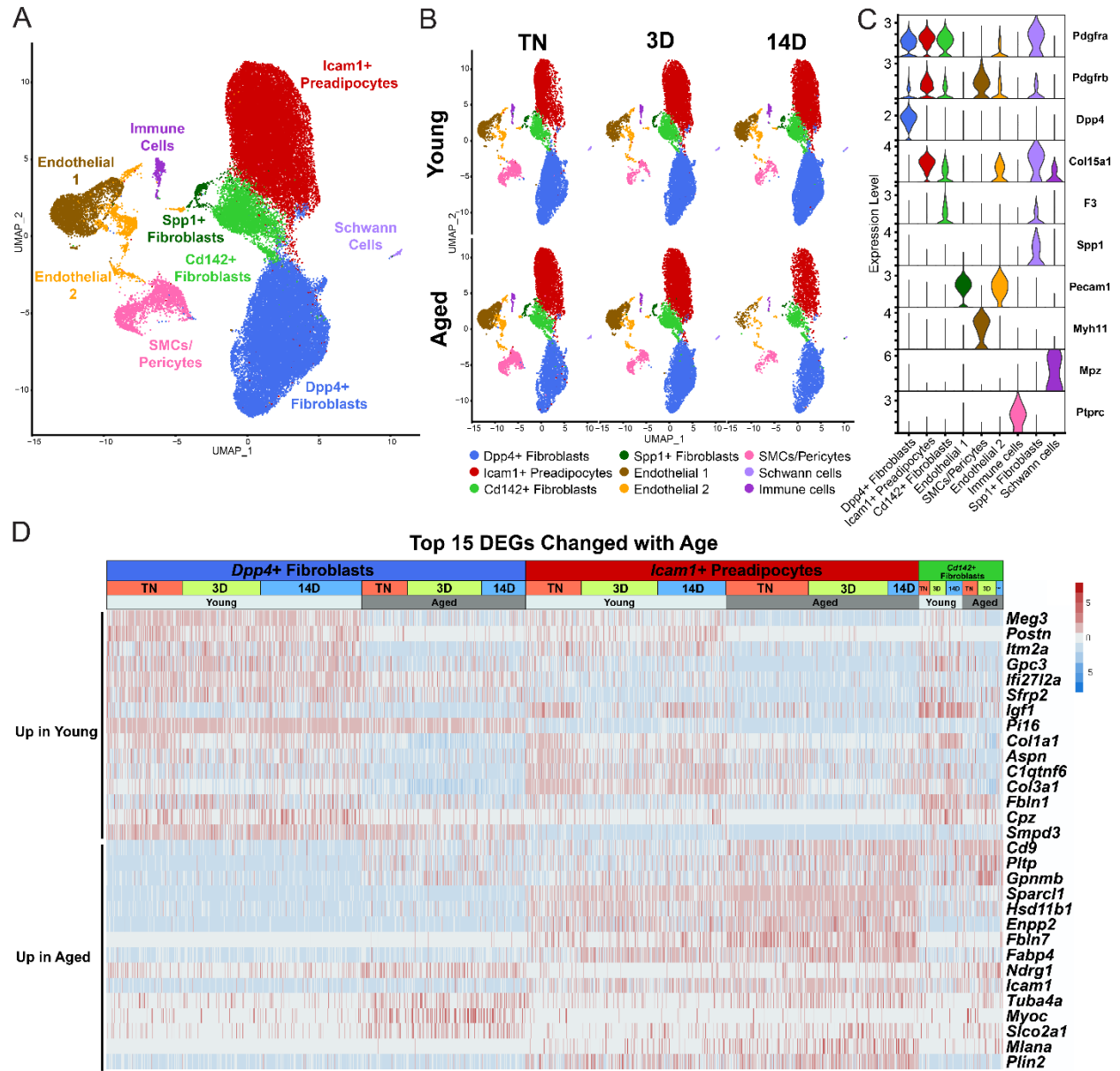
Figure 2. Aging blocks beige adipogenesis from fibroblastic ASPCs.

(A) Schematic of *Pdgfra*^{CreERT2};*R26R*^{tdTomato} reporter mouse model and lineage tracing paradigm. (B) Flow cytometry-based quantification showing proportion of tdTomato-expressing PDGFR α ⁺ cells (as % of total Live, Lin⁻, PDGFR α ⁺ cells) in iWAT from young and aged Cre⁺ and Cre⁻ (control) mice. n=6 young, 5 aged (Circles represent male mice, triangles represent female mice). (C) Immunofluorescence analysis of tdTomato (red), UCP1 (green), PLIN1 (white) and DAPI (blue) in iWAT from young and aged reporter mice after 14 days of 6°C cold exposure (chase). Scale bar 100 μ m. (D) Representative stitched images of full length iWAT histology slices from samples in (C) showing quantification of traced tdTomato⁺;UCP1⁺ multilocular (beige) adipocytes (blue numbers). LN= lymph node, scale bar 500 μ m. (E) Quantification of traced beige adipocytes from (D) presented as total cell number (left) or proportion of PLIN1⁺ area (right), n=7 (young), n=5 (aged). Data represent mean \pm SEM, points represent biological replicates, 2 groups analyzed using a Student's t-test, and multiple conditions analyzed with a Holm-Šidák correction for multiple comparisons. Significance: not significant, P > 0.05; * P < 0.05 ** P < 0.01; *** P < 0.001..

142 **Aging blocks beige adipogenesis from *Pdgfra*⁺ ASPCs**

143 To determine the contribution of fibroblastic ASPCs to beige adipocytes during cold
144 exposure, we performed lineage tracing using *Pdgfra-Cre*^{ERT2};*R26R*^{tdTomato} reporter mice. *Pdgfra*
145 expression marks multiple ASPC populations, including preadipocytes (Merrick et al., 2019;
146 Sakers et al., 2022). Young and aged reporter mice were treated with tamoxifen for 5 days at TN
147 (30°C; "pulse") to activate Cre and induce tdTomato expression in *Pdgfra*⁺ cells. Following a 9
148 day washout period, mice were transferred to 6°C (cold) for two weeks ("chase") (**Figure 2A**). We
149 observed near complete and specific labeling of ASPCs during the pulse period, with ~95% of
150 PDGFR α ⁺ cells in iWAT from young and aged mice displaying tdTomato expression (**Figures 2B,**
151 **S2A**). No tdTomato-expressing adipocytes were observed after the pulse (**Figure S2B**). After 14
152 days of cold exposure, we detected many newly developed beige adipocytes from ASPCs in
153 young mice (visible as tdTomato⁺/UCP1⁺ multilocular adipocytes). By contrast, very few ASPC-
154 derived (tdTomato⁺) were detected in the beige fat areas of aged iWAT at day 14 (**Figures 2C**).
155 Quantifying across the entire length of iWAT pads revealed that most beige adipogenesis
156 occurred in the inguinal region and was ~12-fold lower in aged than in young (**Figure 2D,E**).
157 However, the overall contribution of *Pdgfra*⁺ ASPCs to beige adipocytes was relatively low, even
158 in young animals, with <20% of beige adipocytes expressing tdTomato.

Figure 3



159
160
161
162
163
164
165
166

Figure 3. Single cell expression profiling of ASPCs during iWAT beiging.

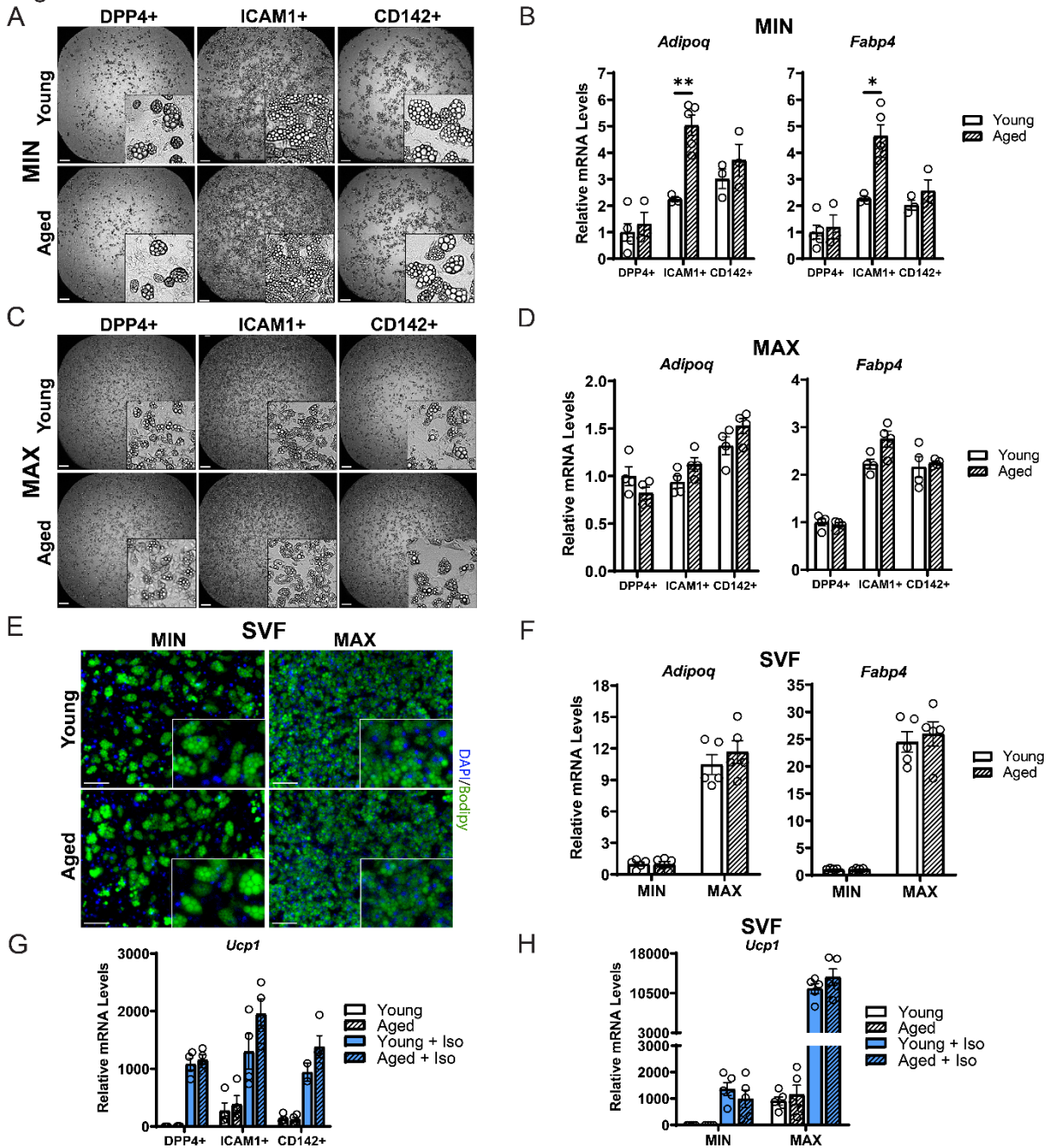
(A) Fully integrated UMAP of gene expression in 54,987 stromal vascular cells (FACS depleted of CD45⁺ immune cells) from young and aged mouse groups detailed in Figure 1A. (B) UMAPs split by condition. (C) Violin plots showing the expression levels of representative marker genes for various cell clusters. y-axis = log-scale normalized read count. (D) Expression heatmap of the top differentially expressed genes in young vs. aged fibroblastic ASPCs (combined *Dpp4*⁺, preadipocytes and *Cd142*⁺ cells). Table shows expression of these genes in ASPC populations across temperature conditions (TN, cold 3D, cold 14D) from young and aged mice.

167 **Single cell expression profiling of ASPCs**

168 We previously identified three main fibroblastic ASPC populations in iWAT: DPP4⁺
169 interstitial cells, ICAM1⁺ preadipocytes, and CD142⁺ cells. All these cell types express *Pdgfra* and
170 have the capacity to undergo adipogenic differentiation (Merrick et al., 2019). We hypothesized
171 that the aging-related impairment of beige adipogenesis was caused by dysregulation of these
172 ASPC types. To investigate this, we performed scRNA-seq on stromal vascular cells from iWAT
173 of young and aged animals, maintained at TN, or following transition to cold for 3 or 14 days
174 (**Figure 1A**). ASPCs were enriched by removing immune (CD45⁺) cells using fluorescence
175 activated cell sorting (FACS). We integrated the datasets from all conditions together and
176 performed clustering analysis. The following cell populations were annotated based on their
177 expression of cell type-specific marker genes: four fibroblast populations (*Dpp4*⁺; *Icam1*⁺
178 preadipocytes; *Cd142*⁺, *Spp1*⁺), two populations of endothelial cells (*Pecam1*⁺); smooth muscle
179 cells/pericytes (*Myh11*⁺, *Pdgfrb*⁺); Schwann cells (*Mpz*⁺); and residual immune cells (*Ptprc*⁺)
180 (**Figures 3A-C**). Aging or cold exposure did not promote the emergence of any specific cell
181 populations. In this regard, we did not identify ‘aging-dependent regulatory cells (ARCs)’, which
182 were previously defined as ASPCs expressing *Lgals3* and other inflammatory genes (**Figure**
183 **S3A**) (Nguyen et al., 2021). The expression levels of identity markers of the ASPC populations
184 were not modulated during cold exposure or aging (**Figure S3B**).

185 Differential gene expression analyses identified aging-modulated genes in the ASPC
186 populations (**Figure 3D**). Notably, expression of *Cd9*, previously identified as a fibrogenic marker,
187 was upregulated with age in *Dpp4*⁺ cells and preadipocytes (Marcelin et al., 2017). *Pltp* and
188 *Gpnmb* were also elevated by aging across all ASPC populations and temperature conditions.
189 Genes downregulated by aging in all ASPC populations included *Meg3*, *Itm2a* and *Gpc3* and
190 *Postn*. Of note, *Postn* encodes an extracellular matrix protein that was previously reported to
191 regulate adipose tissue expansion and decrease in expression during aging (Graja et al., 2018).

Figure 4



192
 193 **Figure 4. ASPCs from young and aged mice display similar beige adipogenic activity ex vivo.** (A, C) Phase contrast
 194 images of DPP4⁺, ICAM1⁺ and CD142⁺ cells from iWAT of young and aged mice that were induced to undergo adipocyte
 195 differentiation with minimal (MIN, A) or maximal (MAX, C) induction cocktail for 8 days. Scale bar 200 μ m. (B, D) mRNA levels
 196 of adipocyte marker genes *Adipoq* and *Fabp4* in cultures from (A, C). Data points represent separate wells, sorted from a pool
 197 of 5 mice (A) or sorted from two pools of 2-3 mice (C). (E) Stromal vascular fraction (SVF) cell cultures from the iWAT of young
 198 and aged mice were induced to differentiate for 8 days with MIN or MAX cocktail, followed by Bodipy (green) staining of lipid
 199 droplets and DAPI (blue) staining of nuclei. Scale bar 100 μ m. (F) Relative mRNA levels of *Adipoq* and *Fabp4* in cultures from
 200 (E). Data points represent wells from individual mice, n = 5. (G, H) Relative mRNA levels of *Ucp1* in adipocyte cultures from
 201 (C, E) with or without treatment with isoproterenol for 4 hours. Data points represent wells sorted from two pools of 2-3 mice

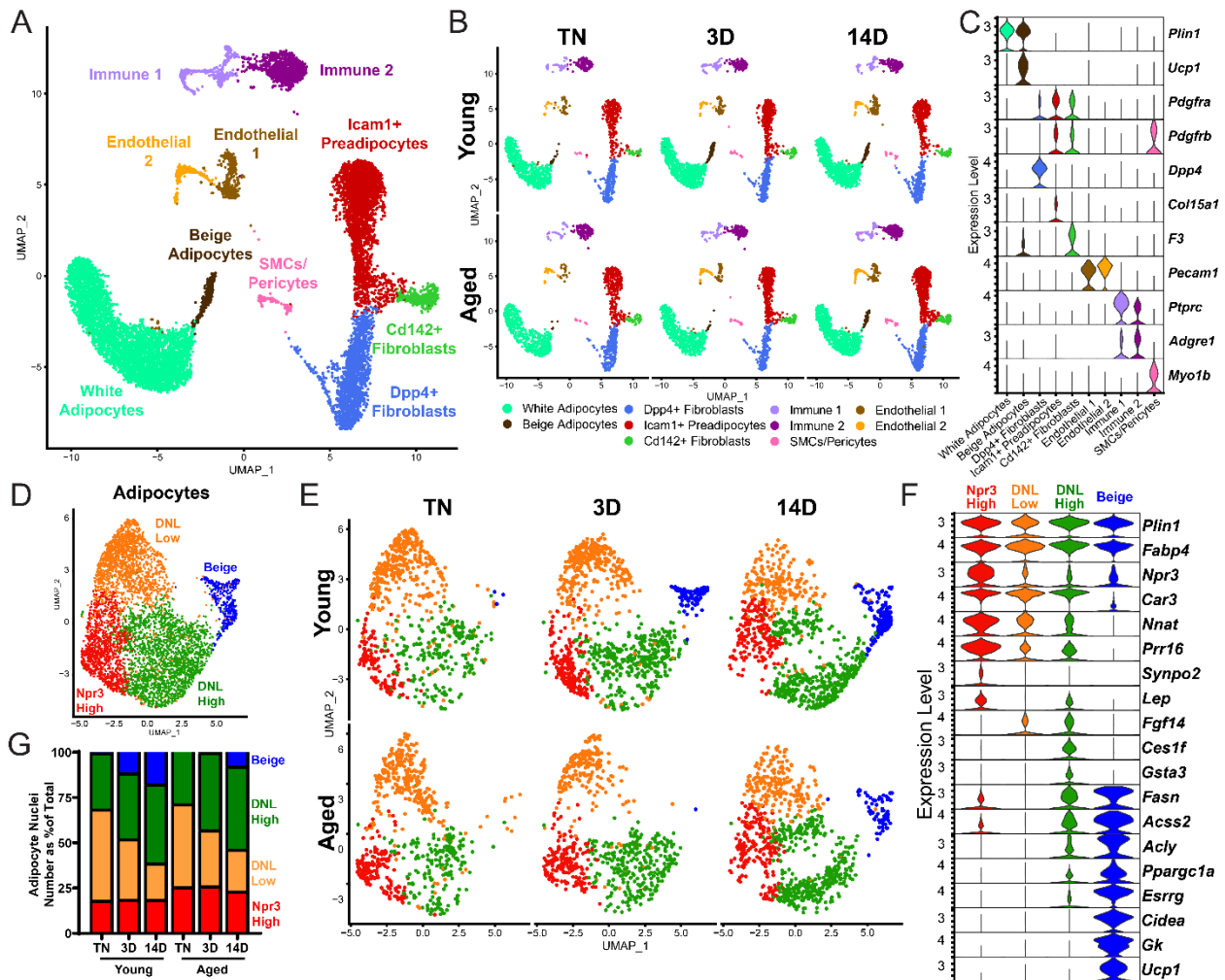
202 (G) or wells from individual mice, n=5 (H). Data represent mean \pm SEM, 2 groups analyzed using a Student's t-test, and
203 multiple conditions analyzed with a Holm-Šidák correction for multiple comparisons. Significance: not significant, $P > 0.05$; *
204 $P < 0.05$ ** $P < 0.01$; *** $P < 0.001$.

205

206 **ASPCs from aged mice are competent for beige adipogenesis ex vivo**

207 We next evaluated if ASPCs from young and aged animals exhibit cell-autonomous
208 differences in adipogenic differentiation capacity. We FACS-purified the three ASPC populations,
209 DPP4⁺, ICAM1⁺ and CD142⁺ cells, from the iWAT of young and aged mice, plated them in culture
210 and induced adipocyte differentiation. Using a minimal differentiation stimulus consisting of insulin
211 only (MIN), ICAM1⁺ and CD142⁺ cells underwent more efficient differentiation into lipid droplet-
212 containing adipocytes, and expressed higher levels of adipocyte genes (*Adipoq* and *Fabp4*) than
213 DPP4⁺ cells, consistent with prior work (**Figures 4A,B**) (Merrick et al., 2019). DPP4⁺ and CD142⁺
214 cells from young and aged mice underwent adipocyte differentiation and induced adipocyte genes
215 with equivalent efficiency. Unexpectedly, aged ICAM1⁺ cells exhibited greater differentiation
216 capacity than young ICAM1⁺ cells, as evidenced by higher expression levels of *Adipoq* and *Fabp4*
217 (**Figures 4A,B**). Maximal stimulation with a full cocktail of adipogenic inducers (MAX), produced
218 similar and robust differentiation in all ASPC populations from young or aged mice (**Figures**
219 **4C,D**). To assess whether young and aged precursor cells behave differently when cultured as a
220 mixed heterogeneous population, we isolated the stromal vascular fraction (SVF) for
221 adipogenesis assays. Again, SVF cell cultures from both young and aged mice displayed similar
222 adipogenic differentiation capacity with either MIN or MAX stimulation (**Figures 4E,F**). Finally, we
223 stimulated cell cultures with the pan-adrenergic agonist isoproterenol for 4 hours to evaluate
224 thermogenic gene activation (i.e., beiging). Basal levels of *Ucp1* expression appear to be lower in
225 DPP4⁺ cells compared to other ASPC types, but all three ASPC populations activated *Ucp1*
226 expression to high and similar levels in response to stimulation and did not differ by age (**Figure**
227 **4G**). We also did not observe an aging-related difference in the levels of *Ucp1* induction in SVF-
228 derived adipocyte cultures stimulated with either MAX or MIN cocktail, and as expected, MAX
229 differentiated cells demonstrated greater stimulated capacity (**Figure 4H**). Together, these data
230 suggest that the beige adipogenic capacity of ASPCs is not intrinsically compromised in aged
231 mice, and therefore the *in vivo* deficit in beige adipogenesis could be due to non-ASPC-
232 autonomous effects.

Figure 5



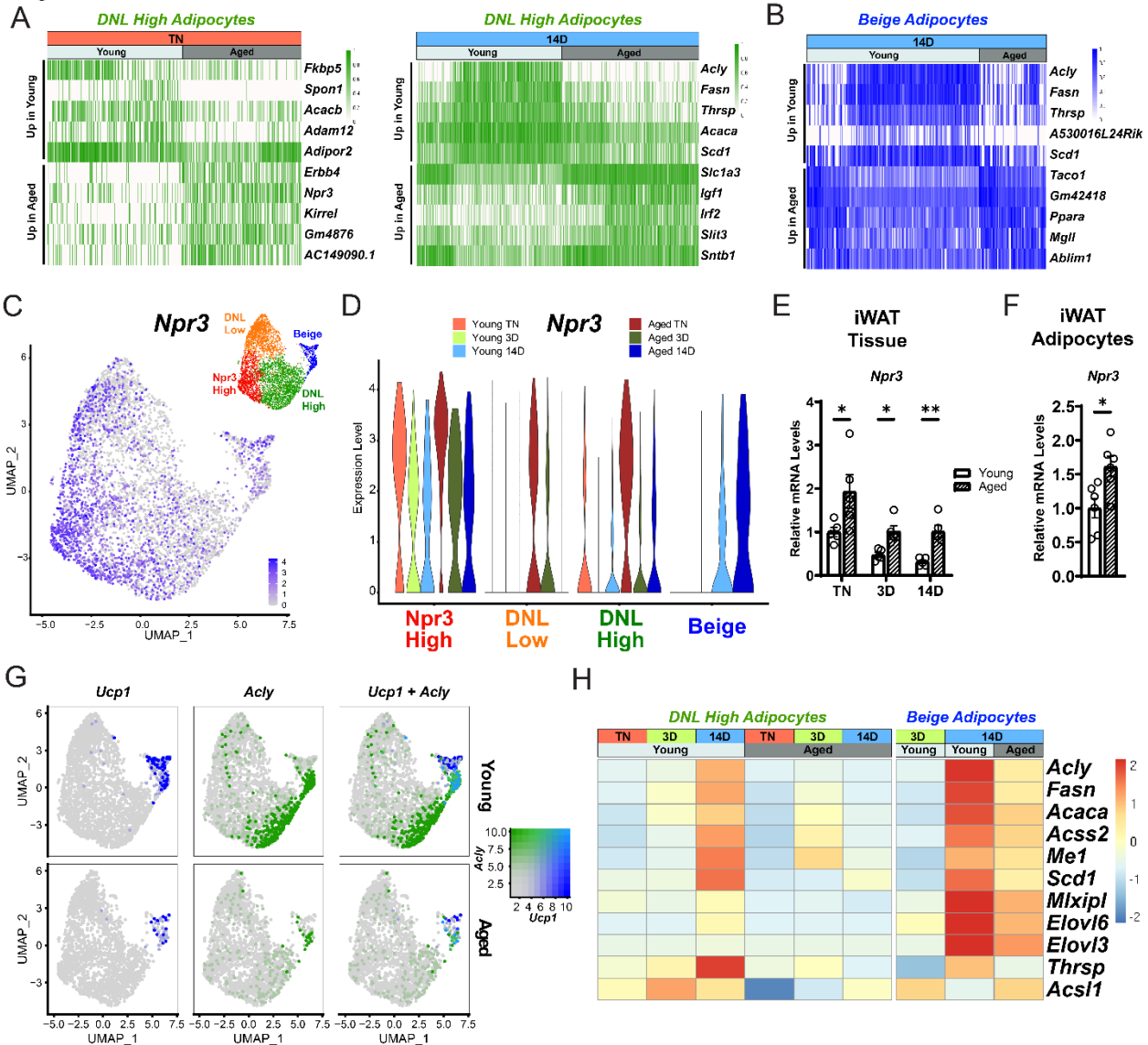
233
 234 **Figure 5. Single nucleus expression profiling of adipocytes during the beiging process in young and aged mice. (A)**
 235 Fully integrated UMAP of mRNA levels in 11,905 nuclei from iWAT of mouse groups detailed in Figure 1A, n=2 mice per
 236 condition. **(B)** UMAPs split by condition. **(C)** Violin plots showing expression patterns of cell cluster-selective marker genes,
 237 Y-axis = log-scale normalized read count. **(D)** UMAP of gene expression in re-integrated adipocyte clusters including 4,937
 238 nuclei from (A) identifying four populations: Npr3-high, beige, DNL-low, and DNL-high. **(E)** Adipocyte UMAPs split by condition.
 239 **(F)** Violin plots showing expression patterns of selected genes in adipocyte populations, Y-axis = log-scale normalized read
 240 count. **(G)** Adipocyte nuclei numbers in each sample, plotted as percent of total adipocytes captured for that sample.

241 **Single nucleus RNA sequencing uncovers adipocyte heterogeneity**

242 To determine the effects of aging and cold exposure on adipocyte gene profiles, we
243 performed snRNA-seq analyses of iWAT samples using the same experimental paradigm
244 described above (**Figure 1A**). We integrated all the conditions together for analyses from two
245 separate runs. Similar cell types were captured as with scRNA-seq (**Figure 3A**), but with the
246 addition of mature adipocyte populations (**Figure 5A**). This dataset has increased representation
247 from immune cells since there was no negative selection against CD45⁺ cells. As with the single-
248 cell data set, we did not identify any aging-specific cell populations (**Figure S4A**). However, we
249 observed striking differences in the adipocyte cluster across age and temperature. Most obvious
250 was the emergence and expansion of a distinct beige adipocyte population, marked by expression
251 of *Ucp1* and other thermogenic genes, during cold exposure (**Figure 5B**).

252 To focus on adipocyte responses, we reintegrated the snRNA-seq data using only the
253 adipocytes, which revealed four main clusters (**Figures 5D-F**). Beige adipocytes, marked by high
254 expression of many thermogenic genes (i.e., *Ppargc1a*, *Esrrg*, *Cidea*, *Gk* and *Ucp1*), were the
255 most distinctive cluster and were largely absent at TN in young and aged mice, but they began to
256 appear in young mice after 3 days of cold exposure, and were further increased at 14 days. By
257 contrast, in aged mice, beige cells were barely detectable at 3 days of cold exposure and were
258 present at greatly reduced numbers than in young mice at 14 days (**Figure 5E**). This analysis
259 also revealed three sub-populations of 'white' adipocytes. 'Npr3-high' adipocytes were enriched
260 for expression of *Npr3*, *Synpo2*, *Prr16*, and *Tshr*, expressed higher levels of canonical white fat
261 marker genes *Leptin* (*Lep*) and *Nnat*, and exhibited the lowest expression levels of thermogenic
262 (beige) genes. Two additional white adipocyte clusters were designated as 'de novo lipogenesis
263 (DNL)-low' and 'DNL-high' cells, both of which expressed lower levels of *Npr3* and shared
264 selective expression of *Fgf14*. DNL-high cells uniquely expressed *Ces1f* and *Gsta3*, and
265 activated high levels of DNL pathway genes (i.e., *Fasn*, *Acss2* and *Acly*) upon cold exposure
266 (**Figure 5F**). Quantification of adipocyte nuclei from this data set showed that the proportions of
267 *Npr3*-high and DNL-high adipocytes remain stable across temperature, with aged mice having
268 more *Npr3*-high adipocytes. The proportion of beige adipocytes increased dramatically during
269 cold exposure selectively in young animals, as expected, while DNL-low adipocytes decreased
270 with cold exposure in both young and aged mice (**Figure 5G**).

Figure 6



271
272
273
274
275
276
277
278
279
280
281
282

Figure 6. Aging blocks activation of the lipogenic gene program in adipocytes

(A) Expression heatmap of the top aging-regulated genes in DNL-high adipocytes at TN (left) and after 14 days of cold exposure (right). (B) Expression heatmap of the top aging-regulated genes in beige adipocytes after 14 days of cold exposure. (C) UMAP of *Npr3* mRNA levels in adipocyte populations (from Figure 5D). (D) Violin plot showing *Npr3* mRNA levels in adipocyte populations, Y-axis = log-scale normalized read count, first bar in beige is 'Young 3D'. (E) *Npr3* mRNA levels in iWAT from mouse groups described in Figure 1A, n=5. (F) *Npr3* mRNA levels in isolated adipocytes from TN-acclimated young and aged mice, n=6. (G) UMAPs of *Ucp1*, *Acly*, and co-expression mRNA levels in adipocyte populations from all young and aged mice. (H) Heatmap showing average expression of lipogenic genes in all nuclei from DNL-high and beige adipocytes per condition indicated in the top table. Data represent mean \pm SEM, points represent biological replicates, 2 groups analyzed using a Student's t-test, and multiple conditions analyzed with a Holm-Šidák correction for multiple comparisons. Significance: not significant, P > 0.05; * P < 0.05 ** P < 0.01; *** P < 0.001.

283 **Aging dysregulates gene programming in adipocyte populations**

284 To evaluate the global effects of cold exposure and aging on adipocytes, we performed
285 differential gene expression analysis between young and aged adipocytes within each cluster.
286 DNL-high and beige adipocytes exhibited the most dramatic expression changes between young
287 and aged animals (**Figures 6A-B, S4B-C**). At TN, DNL-high cells from aged animals expressed
288 lower levels of several genes, including *Fkbp5*, *Spon1* and *Adam12*. Interestingly, *Npr3*, in
289 addition to marking *Npr3*-high cells, was increased by aging in DNL-high adipocytes and to a
290 lesser extent in other adipocyte populations (**Figure 6C,D**). In young animals, *Npr3* expression
291 was downregulated by cold exposure in the three white adipocyte populations, and this
292 downregulation was blunted in aged animals (**Figure 6D**). Gene expression analysis of whole
293 iWAT pads confirmed that *Npr3* mRNA levels are progressively decreased by cold exposure and
294 elevated in aged versus young mice under all temperature conditions (**Figure 6E**). *Npr3*
295 expression levels were also increased in isolated primary adipocytes from aged relative to young
296 mice (**Figure 6F**). Expression levels of the G-protein coupled NP receptors *Npr1* or *Npr2* were
297 not modulated by cold or aging in iWAT or iWAT adipocytes (**Figure S4D,E**).

298 We also observed a striking activation of the DNL and related gene programs (*Acly*, *Fasn*,
299 *Acaca*, *Scd1*, etc.) in DNL-high and beige adipocytes during cold exposure (**Figures 6G,H**). The
300 induction of these genes during cold exposure, exemplified by *Acly* expression, was a cluster-
301 defining attribute of DNL-high cells, which did not express beige genes like *Ucp1* even after 14
302 days of cold exposure. Of note, we found two types of beige (UCP1⁺) adipocytes, distinguished
303 by the presence vs. absence of high DNL gene levels (i.e., UCP1⁺; DNL⁺ and UCP1⁺; DNL(-)), with
304 the latter arising first during cold exposure (3D vs. 14D) (**Figures 6G, S4F,G**). Importantly, the
305 induction of DNL genes was nearly completely blocked in DNL-high cells and reduced in beige
306 cells of aged animals (**Figure 6G**). Indeed, the top aging downregulated genes in adipocytes from
307 cold exposed mice correspond to DNL and related pathways, especially in DNL-high cells (**Figure**
308 **S4I**). Lastly, at the whole tissue level, we observed robust induction of *Acly* in iWAT of young
309 relative to aged mice with increasing duration of cold exposure (**Figure S4H**). Taken together,
310 these results implicate the suppression of natriuretic peptide signaling and DNL in contributing to
311 the aging-related impairment of beige fat formation.

312 Discussion

313 Thermogenic adipose tissue activity declines during aging of mice and humans,
314 correlating with increases in fat mass and susceptibility to cardiometabolic diseases (Berry et al.,
315 2017; Cypess et al., 2009; Pfannenbergl et al., 2010; Rogers et al., 2012; Saito et al., 2009; W.
316 Wang et al., 2019; Yoneshiro et al., 2011). Our study provides a comprehensive unbiased profile
317 of the adipose tissue beiging process and reveals pathways dysregulated by aging in ASPCs and
318 adipocytes during this process.

319 Beige adipocytes develop via the *de novo* differentiation of ASPCs or through activation
320 of the thermogenic gene program in mature adipocytes. Previous studies defined three
321 populations of fibroblastic ASPCs in iWAT, namely *Dpp4*⁺ interstitial cells, *Icam1*⁺ preadipocytes,
322 and *Cd142*⁺ cells (Burl et al., 2018; Merrick et al., 2019). Aging or cold exposure did not induce
323 dramatic shifts in either the proportions, or gene expression signatures of any of these ASPC
324 types, suggesting that these cell populations are stably maintained across a range of conditions.
325 In support of this, aging did not diminish the cell-intrinsic adipogenic capacities of these ASPC
326 populations, when isolated and subjected to adipogenesis assays *ex vivo*. Notably, we did not
327 observe the emergence of aging-dependent regulatory cells (ARCs), previously described as
328 modulated ASPCs co-expressing ASPC and immune marker genes, which have the capacity to
329 suppress adipocyte differentiation (Nguyen et al., 2021). However, we did observe the induction
330 of ARC-selective gene markers (i.e., *Lgals3*, *Cd36*) specifically in immune cells (*Ptprc*⁺, *Adgre1*⁺)
331 from aged mice in both our scRNA-seq and snRNA-seq datasets. This *Lgals3/Cd36* gene
332 signature has also been described in Lin⁺ macrophages and CD45⁺ lipid-associated (LAM)
333 macrophages (Burl et al., 2018; Jaitin et al., 2019). Overall, our results suggest that aging-induced
334 alterations to the systemic milieu or adipose tissue environment are responsible for the block in
335 beige adipogenesis.

336 Gene expression analyses identified several genes that were altered by aging across
337 multiple ASPC types and temperature conditions. The top aging-upregulated gene was *Cd9*,
338 which was previously identified as a marker of fibrogenic (fibrosis-generating) progenitor cells
339 (Marcelin et al., 2017). *Cd9* encodes for a tetraspanin protein implicated in various processes that
340 could affect adipogenesis, including extracellular vesicle production, cell adhesion, inflammation,
341 and platelet activation (Brosseau, Colas, Magnan, & Brouard, 2018). Aging also upregulated the
342 expression of *Pltp* and *Gpnmb*, which are both linked to the regulation of inflammation and fibrosis
343 (Prabata, Ikeda, Rahardini, Hirata, & Emoto, 2021; Saade, Araujo de Souza, Scavone, &
344 Kinoshita, 2021). Conversely, *Meg3*, *Itm2a* and *Postn* were consistently downregulated across all
345 ASPC populations from aged versus young mice. Of note, Periostin (*Postn*) is an extracellular

346 matrix protein that regulates adipose tissue lipid storage, and its levels were previously shown to
347 decrease in several adipose tissue depots during aging (Graja et al., 2018).

348 We were surprised by the limited (<20%) contribution of fibroblastic (*Pdgfra*⁺) ASPCs,
349 (which includes *Pparg*-expressing preadipocytes), to beige adipocytes during cold exposure.
350 Previous studies in mice using an adipocyte fate tracking system show that a high proportion of
351 beige adipocytes arise via the *de novo* differentiation of ASPCs (Q. A. Wang, Tao, Gupta, &
352 Scherer, 2013). However, the relative contribution from ASPC differentiation and direct adipocyte
353 conversion to the formation of beige adipocytes depends highly on the experimental conditions,
354 especially cold exposure history (Shao et al., 2019). Mice housed at TN from birth undergo high
355 rates of *de novo* beige adipogenesis upon first cold exposure, whereas mice reared at room
356 temperature acquire many ‘dormant’ beige adipocytes that can be re-activated by cold exposure
357 (Rosenwald, Perdikari, Rulicke, & Wolfrum, 2013; Shao et al., 2019). Based on these findings,
358 we presume that mature (dormant beige) adipocytes serve as the major source of beige
359 adipocytes in our cold-exposure paradigm. However, long-term cold exposure also recruits
360 smooth muscle cells to differentiate into beige adipocytes; a process that we did not investigate
361 here (Berry, Jiang, & Graff, 2016; Long et al., 2014; McDonald et al., 2015; Shamsi et al., 2021).

362 The beiging process is associated with a dramatic remodeling of adipose tissue structure
363 and metabolic function. We applied snRNA-seq analysis to investigate the cold response of iWAT
364 adipocytes in young and aged animals, leading us to identify four adipocyte clusters: beige
365 adipocytes and three “white” subsets: *Npr3*-high, DNL-low and DNL-high adipocytes. *Npr3*-high
366 adipocytes were enriched for expression of white fat-selective genes and exhibit the lowest levels
367 of thermogenic genes (Rosell et al., 2014; Ussar et al., 2014). Interestingly, *Npr3* also upregulated
368 by aging in all white adipocytes. Previous studies show that obesity also increases *Npr3* levels in
369 adipose tissue of mice and humans (Gentili et al., 2017; Kovacova et al., 2016). NPR3 represses
370 beige fat development and adipocyte thermogenesis by functioning as a clearance receptor for
371 natriuretic peptides (NPs), thereby reducing their lipolytic and thermogenic effects (Bordicchia et
372 al., 2012; Coue et al., 2018; Moro et al., 2004; Sengenès, Berlan, Glisezinski, Lafontan, &
373 Galitzky, 2000; Sengenès et al., 2003). Together, these results suggest that *Npr3*-high adipocytes
374 may impede beige fat development in a cell non-autonomous manner by reducing NP signaling.
375 Moreover, high NPR3 levels in aged animals could contribute to the block in beige fat
376 development, and targeting this pathway may be a promising avenue to elevate beige fat activity.

377 We were also intrigued by the dramatic induction of lipogenesis genes in both beige
378 adipocytes and DNL-high cells during cold exposure. Previous work established that cold
379 stimulates opposing pathways of lipid oxidation and lipogenesis in thermogenic fat tissue (Mottillo

380 et al., 2014; Sanchez-Gurmaches et al., 2018; Yu, Lewin, Forrest, & Adams, 2002). The co-
381 occurrence of these two processes is unusual and may provide a mechanism to ensure the
382 continued availability of fatty acids to fuel thermogenesis and/or provide critical metabolic
383 intermediates, such as acetyl-CoA. The Granneman lab demonstrated that high expression of the
384 lipid catabolic enzyme MCAD and lipogenic enzyme FAS occurred in separate populations of
385 iWAT adipocytes upon stimulation with a β 3-adrenergic agonist for 3-7 days (Lee, Kim, Kwon, &
386 Granneman, 2017). We identified two subsets of UCP1⁺ beige adipocytes, distinguished by the
387 presence vs. absence of high levels of DNL genes (i.e., UCP1⁺; DNL-high and UCP1⁺; DNL-low).
388 Interestingly, the UCP1⁺; DNL-high cells accumulated later during cold exposure (14D),
389 suggesting that fully cold-adapted beige adipocytes express both pathways simultaneously. Of
390 note, the induction of *Acly* and other lipogenic genes was very severely impaired in aged animals.
391 Related to this point, Martinez Calejman and colleagues showed that *Acly* deficiency in brown
392 adipocytes caused a whitened phenotype, coupled with an unexpected and unexplained reduction
393 in *Ucp1* expression (Martinez Calejman et al., 2020). We speculate that high levels of ACLY may
394 be required to support thermogenic gene transcription by supplying and efficiently shuttling acetyl-
395 CoA for acetylation of histones or other factors.

396 In summary, this work shows that aging impairs beige adipogenesis through non-cell-
397 autonomous effects on adipose tissue precursors and by disrupting adipocyte responses to
398 environmental cold exposure. Expression profiling at the single-cell level reveals adipocyte
399 heterogeneity, including two different types of UCP1⁺ beige adipocytes. Finally, aging-
400 dysregulated pathways, including natriuretic peptide signaling and lipogenesis, may provide
401 promising targets for unlocking beige adipocyte development.

402

403 **Acknowledgements**

404 We thank members of the Seale lab for helpful advice and discussions.

405 **Funding:** NIH grants DK120982 and DK121801 to P.S.; T32 HD083185 to C.D.H; T32 DK007314
406 to E.F.; RC2 DK116691 to E.D.R.

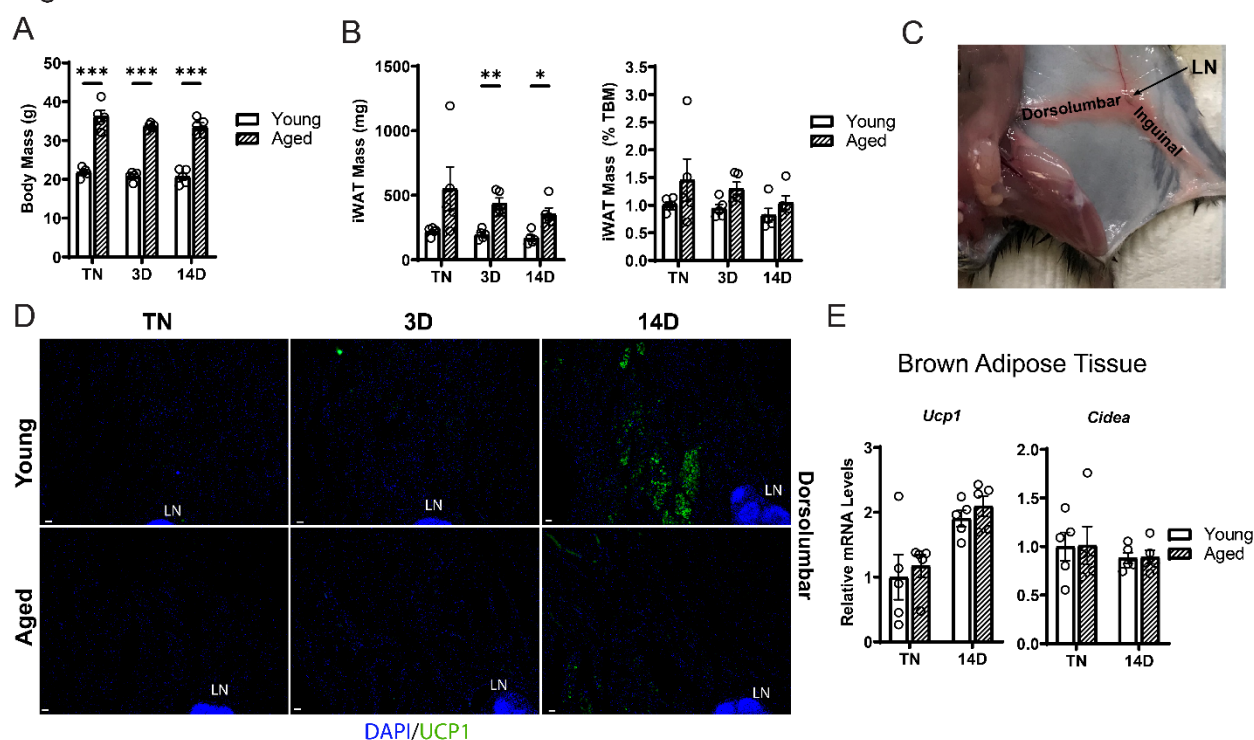
407 **Author Contributions:** C.D.H, A.P.S, R.C. and P.S. were responsible for conceptualization and
408 data analysis. C.D.H and P.S were responsible for writing of the manuscript. C.D.H and A.P.S
409 conducted the majority of the experiments. R.C. and E.F. performed bioinformatics analyses. L.C.
410 processed tissue sections for histology and performed immunostaining. C.J., L.T., and E.D.R.
411 performed and processed the snRNA-seq experiment.

412 **Competing Interests:** The authors declare no competing interests.

413 **Data and materials availability:** scRNA-seq and snRNA-seq datasets are deposited in the Gene
 414 Expression Omnibus (GEO) under the super series accession number GSE227441. Data analysis
 415 pipelines used for processing of raw sequencing data, integration and clustering can be obtained
 416 from: [https://github.com/calhounr/Aging-impairs-cold-induced-beige-adipogenesis-and-](https://github.com/calhounr/Aging-impairs-cold-induced-beige-adipogenesis-and-adipocyte-metabolic-reprogramming)
 417 [adipocyte-metabolic-reprogramming](https://github.com/calhounr/Aging-impairs-cold-induced-beige-adipogenesis-and-adipocyte-metabolic-reprogramming)

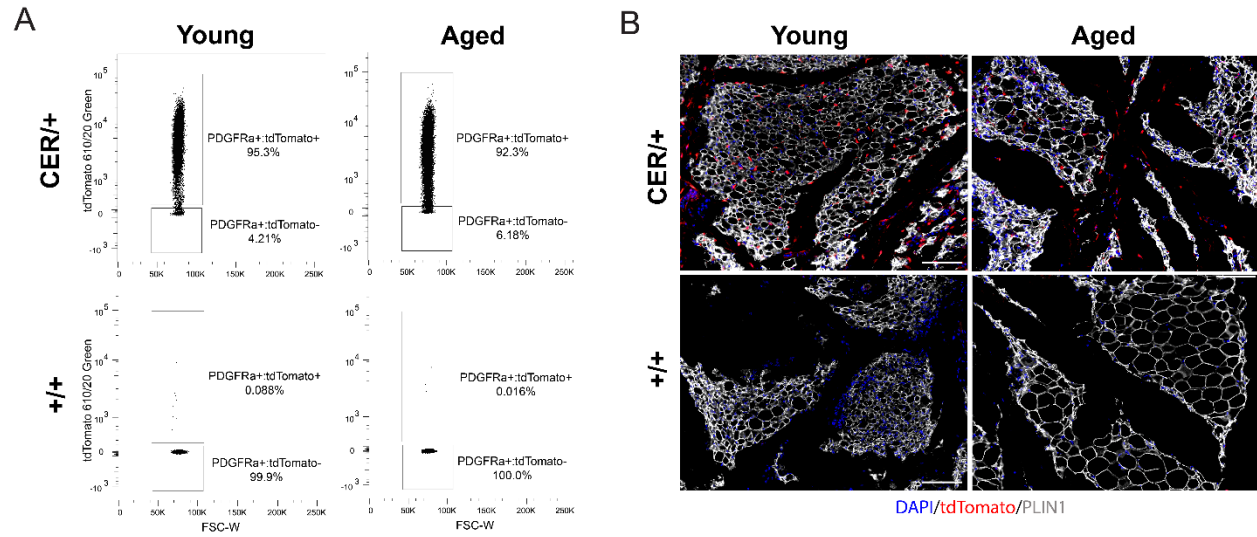
418
 419 **Supplemental Figures**

Figure S1



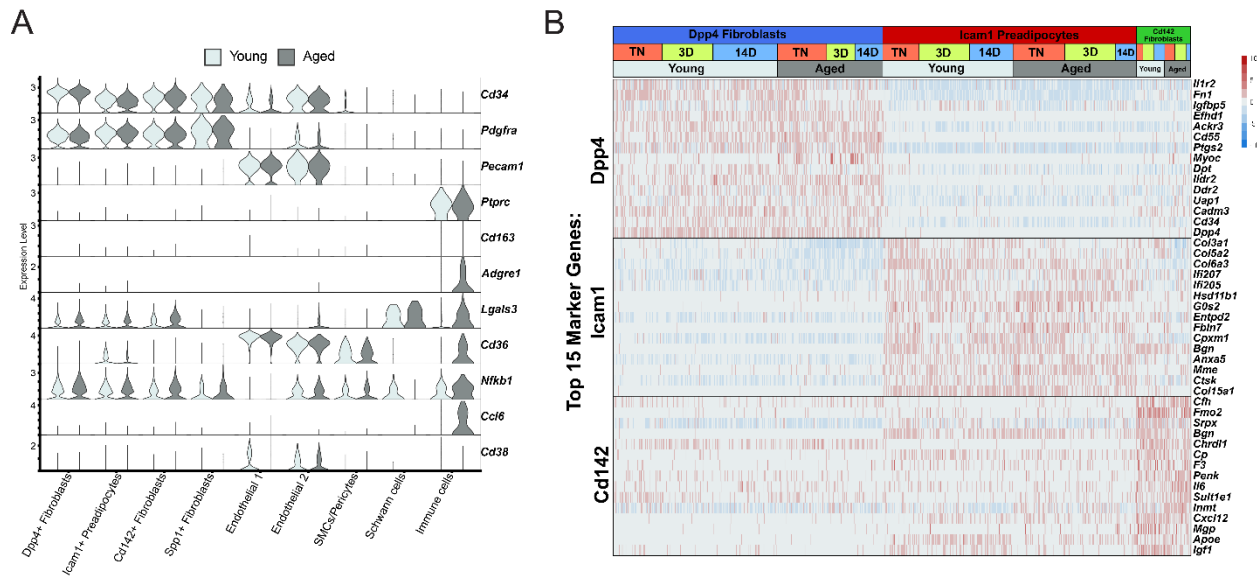
420
 421 **Figure S1, related to Figure 1.** (A-B) Body mass and iWAT mass of mice described in Figure 1A, n=5. (C) Mouse dissection
 422 with lymph node (LN) orientation showing the dorsolumbar and inguinal regions of the iWAT pad. (D) Immunofluorescence
 423 analysis of iWAT with UCP1 (green) and DAPI (blue). LN=lymph node. Scale bar 100 μm. (E) mRNA levels of *Ucp1* and *Cidea*
 424 in BAT of young and aged mice housed at TN, and either maintained at TN or exposed to cold for 2 weeks. Data represent
 425 mean ± SEM, points represent biological replicates, analyzed using a Student's t-test with a Holm-Šidák correction for multiple
 426 comparisons. Significance: not significant, P > 0.05; * P < 0.05 ** P < 0.01; *** P < 0.001.

Figure S2



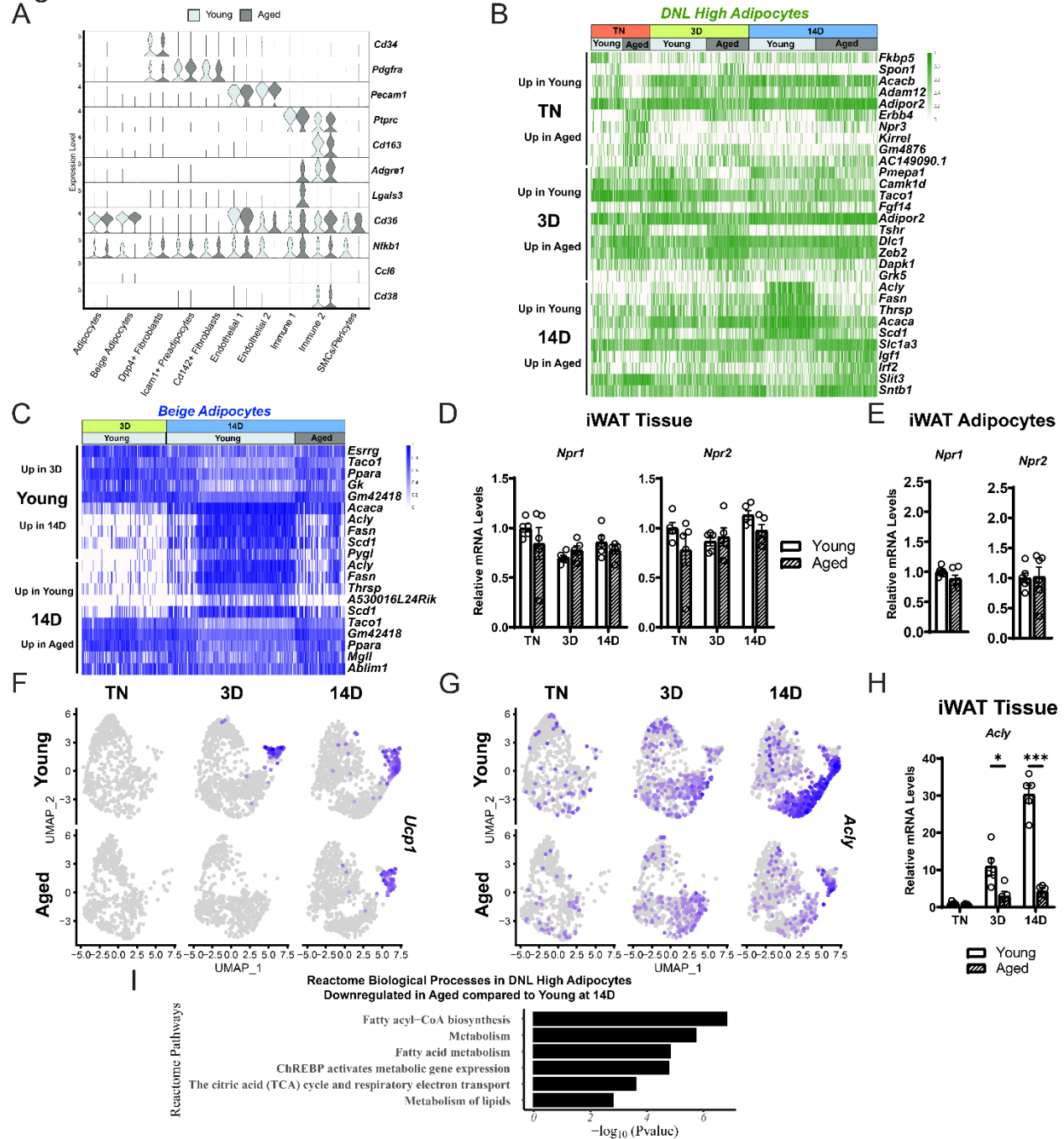
427
 428 **Figure S2, related to Figure 2. (A)** Representative flow cytometry plots showing expression of tdTomato in gated Live, Lin⁻;
 429 PDGFRα⁺ stromal vascular cells isolated from young and aged reporter mice (described in Figure 2) immediately after
 430 treatment with tamoxifen (tmx, pulse). **(B)** Immunofluorescence analysis of iWAT from young and aged reporter mice with
 431 tdTomato (red), PLIN1 (white) and DAPI (blue) after the tmx pulse, scale bar 100 μm.
 432

Figure S3



433
 434 **Figure S3, related to Figure 3. (A)** Violin plot showing expression of ARC marker genes in cell clusters split by age, Y-axis
 435 = log-scale normalized read count. **(B)** Expression heatmap of top ASPC marker genes across age and housing conditions.
 436

Figure S4



437
 438 **Figure S4, related to Figures 5,6.** (A) Violin plot showing expression levels of ARC marker genes split by age, y-axis = log-
 439 scale normalized read count. (B) Expression heatmap of the top aging-regulated genes in DNL-high adipocytes. (C)
 440 Expression heatmap of the top aging-regulated and cold-regulated genes in beige adipocytes. (D-E) *Npr1* and *Npr2* mRNA
 441 levels in (D) iWAT from mouse groups described in Figure 1A, n=5 and (E) isolated adipocytes from iWAT from TN-acclimated
 442 young and aged mice, n=6. (E-F) UMAP of *Ucp1* (E) and *Acly* (F) mRNA levels in adipocyte populations (from Figure 5D). (H)
 443 *Acly* mRNA levels in iWAT from mouse groups described in Figure 1A, n=5. (G) Enrichment analysis displaying the top six
 444 Reactome pathways in DNL high adipocytes downregulated in aged at 14 days. Data represent mean \pm SEM, points represent

445 biological replicates, 2 groups analyzed using a Student's t-test, and multiple conditions analyzed with a Holm-Šidák correction
 446 for multiple comparisons. Significance: not significant, $P > 0.05$; * $P < 0.05$ ** $P < 0.01$; *** $P < 0.001$.

447

448 Materials and Methods

449

Key Resources Table

Reagent type (species) or resource	Designation	Source or reference	Identifiers	Additional information
genetic reagent (M. <i>musculus</i>)	C57BL/6J	The Jackson Laboratory, Bar Harbor, ME	RRID:IMSR_JAX:000664	
genetic reagent (M. <i>musculus</i>)	C57BL/6JN	NIA, Bethesda, MD	NA	
genetic reagent (M. <i>musculus</i>)	Rosa26 loxp-stop-loxp tdTomato Reporter (Ai14)	The Jackson Laboratory, Bar Harbor, ME	RRID:IMSR_JAX:007914	
genetic reagent (M. <i>musculus</i>)	Pdgfra ^{CreERT2}	The Jackson Laboratory, Bar Harbor, ME	RRID:IMSR_JAX:032770	
antibody	Rabbit anti-red fluorescent protein (RFP)	Rockland, Pottstown, PA	600-401-379, RRID:AB_2209751	1:500
antibody	Rabbit anti-Perilipin (D418)	Cell Signaling, Denvers, MA	3470, RRID:AB_2167268	1:200
antibody	Rabbit anti-UCP1	Specially made by AstraZeneca, Cambridge, UK	NA	1:2000
antibody	Anti-mouse CD142	Sino Biological, Chesterbrook, PA	50413- R001	1:100
antibody	Anti-mouse CD142	R & D Systems, Minneapolis, MN	AF3178, RRID:AB_2278143	1:50
antibody	Anti-mouse CD140a-(PDGFR α)-PECy7	Biolegend, San Diego, CA	135912, RRID:AB_2715974	1:100
antibody	Anti-mouse-CD31 (APC-Fire)	Biolegend, San Diego, CA	102528, RRID:AB_2721491	1:1000
antibody	Anti-mouse CD45-allophycocyanin (APC/Cy7)	Biolegend, San Diego, CA	103116, RRID:AB_312981	1:1000
antibody	Anti-mouse ICAM1-phycoerythrin (PE/Cy7)	Biolegend, San Diego, CA	116122, RRID:AB_2715950	1:100
antibody	Anti-mouse CD26 (DPP-4)-fluorescein isothiocyanate (FITC)	Biolegend, San Diego, CA	137806, RRID:AB_10663402	1:200
sequence-based reagent	mTbp	PMID: 24703692	NA	F-GAAGCTGCGGTACAATTCCAG R-CCCCTTGTAACCTTCACCAAT
sequence-based reagent	mAdipoq	PMID: 24703692	NA	F-GCACTGGCAAGTTCTACTGCAA R-GTAGGTGAAGAGAACGGCCTTGT
sequence-based reagent	mFabp4	PMID: 24703692	NA	F-ACACCGAGATTTCTTCAAACCTG R-CCATCTAGGGTTATGATGCTCTTCA

sequence-based reagent	mCidea	PMID: 24703692	NA	F-TGCTCTTCTGTATCGCCCAGT R-GCCGTGTTAAGGAATCTGCTG
sequence-based reagent	mPgc1a	PMID: 24703692	NA	F-CCCTGCCATTGTTAAGACC R-TGCTGCTGTTCTCTGTTTC
sequence-based reagent	mUcp1	PMID: 24703692	NA	F-ACTGCCACACCTCCAGTCATT R-CTTTGCCTCACTCAGGATTGG
sequence-based reagent	mDio2	PMID: 24703692	NA	F-CAGTGTGGTGACGCTCCAATC R-TGAACCAAAGTTGACCACCAG
sequence-based reagent	mAcly	PMID: 31141698	NA	F-GAGTGTCTATTGCGCTTCCC R-GGTTGCCGAAGTCACAGGT
sequence-based reagent	mNpr3	This Paper	NA	F-TTTTCAGGAGGAGGGGTTGC R-ACACATGATCACCCTCGCT
sequence-based reagent	mNpr1	MGH PrimerBank	Primer Bank ID: 113930717c1	F-GCTTGTGCTCTATGCAGATCG R-CCTCGACGAACTCCTGGTG
sequence-based reagent	mNpr2	MGH PrimerBank	Primer Bank ID: 118129825c2	F-CATGACCCCGACCTTCTGTTG R-CGAACCAGGGTACGATAATGCT
commercial assay or kit	ABI High-Capacity cDNA Synthesis kit	Applied Biosystems, Waltham, MA	4368813	
commercial assay or kit	Purelink RNA Mini columns	Invitrogen, Waltham, MA	LT-12183018	
commercial assay or kit	TSA TMR Tyramide Reagent Pack	Akoya Biosciences, Marlborough, MA	NEL742001KT	
commercial assay or kit	TSA Fluorescein Tyramide Reagent Pack	Akoya Biosciences, Marlborough, MA	NEL741001KT	
commercial assay or kit	Bulls Eye Decloaking Buffer	Biocare, Pacheco, CA	BULL1000 MX	
commercial assay or kit	AbC Total Antibody Compensation Bead Kit	BioLegend, San Diego, CA	A10497	
commercial assay or kit	Biotium Mix-n-Stain CF647	Sigma, Burlington, MA	MX647S100	
commercial assay or kit	PicoPure RNA Isolation Kit	Invitrogen, Waltham, MA	KIT0204	
commercial assay or kit	Qubit dsDNA High Sensitivity assay kit	ThermoFisher, Waltham, MA	Q32851	
commercial assay or kit	DNA High Sensitivity Bioanalyzer Chip (Agilent)	Agilent, Santa Clara, CA	5067-4626	
software, algorithm	Graphpad Prism	Graphpad, San Diego, CA	RRID:SCR_002798	
software, algorithm	Adobe Illustrator	Adobe, San Jose, CA	RRID:SCR_010279	
software, algorithm	Adobe Photoshop	Adobe, San Jose, CA	RRID:SCR_014199	
software, algorithm	Image J	PMID: 22743772	RRID:SCR_003070	
software, algorithm	Cell Ranger	10x Genomics	RRID:SCR_017344	
software, algorithm	Seurat	PMID: 34062119	RRID:SCR_016341	
software, algorithm	bcl2fastq	Illumina	RRID:SCR_015058	
software, algorithm	Cumulus	PMID: 32719530	RRID:SCR_021644	

software, algorithm	FACSDiva Softward	Becton Dickinson, Franklin Lakes, NJ	RRID:SCR_001456	
other	Tamoxifen (Free Base)	Sigma, Burlington, MA	T5648	
other	Corn Oil	Sigma, Burlington, MA	C8267	
other	16% Paraformaldehyde	EMS, Hatfield, PA	15710	
other	TRIzol	Invitrogen, Waltham, MA	15596018	
other	CL-316,243	Sigma, Burlington, MA	C5976	
other	4',6-Diamidine-2'-phenylindole dihydrochloride (DAPI), 1:10,000	Roche, Basel, Switzerland	10236276001	
other	Bovine Serum Albumin, fraction V, fatty-acid free	Gold Biotechnology, St. Louis, MO	A-421-250	
other	DMEM/F12	Fisher Scientific, Waltham, MA	11320033	
other	Fetal Bovine Serum	Omega Scientific, Tarzana, CA	FB-11, Lot 401714	
other	Primocin	InvivoGen, San Diego, CA	ant-pm-2	
other	PCR Master Mix, Power SYBR Green	Applied Biosystems, Waltham, MA	4367659	
other	HBSS, 1X	Fisher Scientific, Waltham, MA	14175079	
other	Dispase II	Roche, Basel, Switzerland	4942078001	
other	Collagenase, Type 1	Worthington, Lakewood, NJ	LS004197	
other	Red Blood Cell Lysis Buffer, 10x	BioLegend, San Diego, CA	420302	
other	Human Insulin, Novolin	Novo Nordisk, Bagsvaerd, Denmark	183311	
other	Dexamethasone	Sigma-Aldrich, Burlington, VT	D4902	
other	3-isobutyl-1-methylxanthine (IBMX)	Sigma-Aldrich, Burlington, VT	I7018	
other	Rosiglitazone	Cayman Chemical, Ann Arbor, MI	11884	
other	Indomethacin	Sigma-Aldrich, Burlington, VT	I8280	
other	3,30,5-Triiodo-L-thyronine sodium salt (T3)	Sigma-Aldrich, Burlington, VT	T6397	
other	isoproterenol	Sigma-Aldrich, Burlington, VT	I6504	
other	Biodipy 493/503	Invitrogen, Waltham, MA	D3922	
other	Hoechst 33342	Thermo Fisher, Waltham, MA	62249	
other	Protector RNase Inhibitor	Roche, Basel, Switzerland	3335399001	

451 **Mice**

452 All animal procedures were approved and performed under the guidance of the University of
453 Pennsylvania Institutional Animal Care and Use Committee. Young (4 weeks) and aged (52
454 weeks) C57BL/6 male mice were obtained from the National Institute of Aging (C57BL/6JN) or
455 Jackson Laboratories (C57BL/6J, stock number 000664). Mice were housed at 30°C for 3 weeks,
456 then were either: maintained at 30°C for 2 weeks (TN); kept at 30°C for 11 more days before
457 moving to 6°C for 3 days (3D cold) or moved to 6°C for 14 days (14D cold). Mice were single
458 housed during the final two week temperature treatment and provided with a nestlet and shepherd
459 shack. For experiments with CL316,243 (CL, Sigma-C5976), mice were housed at 30°C for 5
460 weeks, followed by intraperitoneal (IP) injection of 1 mg/kg/d CL either 1 hour prior to tissue
461 harvest or for 5 days. *Pdgfra*^{CreERT2} mice were obtained from Dr. Brigid Hogan (Duke University)
462 (Chung, Bujnis, Barkauskas, Kobayashi, & Hogan, 2018) and crossed with *Rosa26*^{tdTomato} (strain:
463 B6.Cg-Gt(ROSA)26Sortm14(CAG-tdTomato)Hze/J, stock no. 007914). To induce Cre activity,
464 tamoxifen (Sigma, T5648) dissolved in corn oil (Sigma, C8267) was injected intraperitoneally (IP)
465 into mice at a dose of 100 mg/kg/d for 5 days. For all iWAT processing other than histology, the
466 inguinal lymph node was removed.

467

468 **Histology and Immunofluorescence**

469 Tissues were fixed overnight in 4% paraformaldehyde, washed with PBS, dehydrated in ethanol,
470 paraffin-embedded and sectioned. Following deparaffinization, slides were subjected to heat
471 antigen retrieval in a pressure cooker with Bulls Eye Decloaking buffer (Biocare), unless otherwise
472 noted. Slides were incubated in primary antibody overnight and secondary antibody conjugated
473 to peroxidase and then developed using Tyramide Signal Amplification (TSA, Akoya Biosciences).
474 Samples were stained with the following antibodies: anti-red fluorescent protein (RFP) (rabbit;
475 1:500; Rockland #600-401-379), anti-UCP1 (rabbit, 1:2000, AstraZeneca), and anti-PLIN1 (rabbit,
476 1:200 Cell Signaling #3470). Slides were imaged on an inverted fluorescence microscope
477 (Keyence BZ-X710). For quantification of tdTomato-expressing adipocytes, full-length iWAT
478 slices were tile imaged, stitched, exported as a BigTiff, and quantified using the Count Tool in
479 Photoshop (Adobe).

480

481 **Isolation of stromal vascular cells (SCVs) and adipocytes**

482 SVCS. As previously described (Merrick et al 2019, Wang et al 2019), iWAT tissue was dissected,
483 minced gently and digested with Collagenase Type I (1.5 units/ml; Worthington) and Dispase II
484 (2.4 units/ml; Roche) in DMEM/F12 containing 1% fatty acid-free bovine serum albumin (Gold

485 Biotechnology) in a gentleMACS dissociator (Miltenyi Biotec) on program “37 MR ATDK-1.” The
486 digestion was quenched with DMEM/F12 containing 10% FBS, and the dissociated cells were
487 passed through a 100 µm filter and spun at 400 x g for 4 mins. The pellet was resuspended in red
488 blood cell lysis buffer (BioLegend), incubated for 4 mins at RT, then quenched with DMEM/F12
489 containing 10% serum. Cells were passed through a 70 µm filter, spun, resuspended, then passed
490 through a final 40 µm filter, spun at 400 x g for 4 minutes and plated or underwent further
491 processing for FACS. Mice were not pooled unless indicated.

492 Adipocytes. Tissue went through the same process as above, except after digestion and
493 quenching, adipocyte/SVF slurry was filtered through a 200 µm filter and centrifuged at 50 x g for
494 3 mins at RT. Using a 20 mL syringe and 1.5-inch, 25G needle, media containing the SVCs was
495 removed from below the adipocytes (and saved if concurrently isolating SVCs), leaving only the
496 adipocytes in the tube. Adipocytes were washed twice with the same media as quenching,
497 transferred to 2 mL tubes, spun a final time, media was removed from below the adipocytes again,
498 and TRIzol was added for RNA extraction. Mice were not pooled.

499

500 **FACS**

501 DPP4⁺, ICAM1⁺, and CD142⁺ cells were isolated as previously described (Merrick et al 2019).
502 Briefly, SVCs from the subcutaneous adipose of mice (n= 2-5) were pooled and resuspended in
503 FACS buffer (HBSS containing 3% FBS; Fisher), then incubated for 1 hr at 4°C with the following
504 antibodies: CD26 (DPP4)-fluorescein isothiocyanate (FITC) (Biolegend, 137806; 1:200), anti-
505 mouse ICAM1-phycoerythrin (PE)/Cy7 (Biolegend, 116122; 1:100), anti-mouse CD45-
506 allophycocyanin (APC)/Cy7 (Biolegend, 103116; 1:1000), anti-mouse CD31-APC-Fire
507 (Biolegend, 102528; 1:1000), and anti-mouse CD142 (Sino Biological, 50413-R001, 1:100; or
508 R&D Systems, AF3178, 1:50). Anti-mouse CD142 antibodies were conjugated with Biotium Mix-
509 n-Stain CF647 (Sigma, MX647S100). For lineage tracing pulse analysis, SVCs were isolated from
510 individual mice without pooling. SVCs were stained with anti-mouse CD31, anti-mouse CD45,
511 and anti-mouse CD140a (PDGFRA) (PE/Cy7) (Biolegend, 135912; 1:100). In all FACS
512 experiments, cells were stained with 4',6-diamidino-2-phenylindole (DAPI) (Roche, 10236276001;
513 1:10,000) for 5 minutes, then washed three times with FACS buffer to remove unbound
514 antibodies. Cells were sorted with a BD FACS Aria cell sorter (BD Biosciences) equipped with a
515 100 µm nozzle and the following lasers and filters: DAPI, 405 and 450/50 nm; FITC, 488 and
516 515/20 nm; mTomato, 532 and 610/20 nm; PE/Cy7, 532 and 780/60 nm; CF647, 640 and 660/20
517 nm; and APC/Cy7 and APC-Fire, 640 and 780/60 nm. All compensation was performed at the

518 time of acquisition in Diva software by using compensation beads (BioLegend, A10497) for single-
519 color staining and SVCs for negative staining and fluorescence (DAPI and tdTomato).

520

521 **Cell culture and differentiation**

522 *Adipocyte precursor cells*. All cells were cultured in DMEM/F12 containing 10% FBS and Primocin
523 (50 ng/ml) (InvivoGen, ant-pm-1). DPP4⁺, ICAM1⁺, and CD142⁺ populations were FACS purified,
524 plated on CellBind 384-well plates (Corning) at 15-25K cells/well, and incubated for 48 (25K cells)
525 to 72 hours (15K cells) to facilitate attachment before the induction of adipogenic differentiation.
526 For whole SVF, SVCs were isolated and plated in a 48 well CellBind plate (Corning) at a high
527 confluency of one mouse per 18 wells. No cells were passaged after plating to maintain
528 adipogenic competency. Differentiation was carried out with either maximum adipogenic cocktail,
529 max: 500 μ M isobutylmethylxanthine (Sigma, I7018), 10 μ M dexamethasone (Sigma, D4902),
530 125 μ M indomethacin (Sigma, I8280), 1 μ M rosiglitazone (Cayman Chemical, 11884), 1 nM T3
531 (Sigma, T6397), and 20 nM insulin (Novolin) or a minimal adipogenic cocktail, min: 20 nM insulin.
532 For the max adipogenic cocktail induction, cells were incubated with cocktail for 2 days and then
533 transferred to adipogenic maintenance medium for the remaining 6 days (1 μ M rosiglitazone, 1
534 nM T3, and 20 nM insulin). For all conditions, medium was changed every 2 days, and cells were
535 harvested on day 8 of differentiation. For drug treatments, cells were treated for 4 hrs on day 8
536 with 1 μ M isoproterenol (Sigma, I6504). Adipogenesis was assessed by staining with Biodipy
537 493/503 (Invitrogen, D3922) for lipid droplet accumulation and Hoechst 33342 (Thermo Fisher,
538 62249) for nuclei number. The cells were imaged on a Keyence inverted fluorescence microscope
539 (BZ-X710) by using DAPI (excitation, 360/40 nm; emission, 460/50 nm) and green fluorescent
540 protein (excitation, 470/40 nm; emission, 525/50 nm) filters. Individual wells were imaged in their
541 entirety at 4x magnification, and at 20x to see morphology. 384-well plates were not stained and
542 imaged in brightfield due to low cell number recovery from FACS prior to RNA extraction.

543

544 **RNA Extraction, qRT-PCR and RNA Sequencing**

545 *RNA Extraction*. Total RNA was extracted using TRIzol (Invitrogen) combined with PureLink RNA
546 Mini columns (Thermo Fisher, 12183025) for tissue and SVC cells or by PicoPure RNA Isolation
547 Kit (Applied Biosystems, KIT0204) for 384-well plate populations and adipocytes. Prior to the
548 addition of chloroform, all tissue and primary adipocytes in TRIzol included an extra spin at max
549 speed for 10 minutes at RT, then TRIzol was removed from below the lipid layer to avoid lipid
550 contamination disrupting the subsequent phase separation with chloroform. Chloroform was
551 added to the lipid-free TRIzol, spun for 15 mins at 12,000 x g and the aqueous layer was removed

552 and added to columns. mRNA was quantified using a Nanodrop and reverse transcribed to cDNA
553 using the ABI High-Capacity cDNA Synthesis kit (ABI, 4368813). Real-time PCR was performed
554 on a QuantStudio5 qPCR machine using SYBR green fluorescent dye (Applied Biosystems). Fold
555 changes were calculated using the ddCT method, with TATA binding Protein (*Tbp*) mRNA serving
556 as a normalization control.

557

558 Single Cell RNA-seq Samples. Cells were flow sorted to isolate live (DAPI⁻) cells and remove
559 debris. We enriched non-immune cells by sorting out CD45⁺ cells. Next-generation sequencing
560 libraries were prepared using the Chromium Next GEM Single Cell 3' Reagent kit v3.1 (10x
561 Genomics, 1000121) per manufacturer's instructions. Libraries were uniquely indexed using the
562 Chromium Single Index Kit T Set A, pooled, and sequenced on an Illumina NovaSeq 6000
563 sequencer in a paired-end, dual indexing run by the CHOP Center for Applied Genomics at the
564 University of Pennsylvania. Sequencing for each library targeted 20,000 mean reads per cell.

565

566 Single Nucleus RNA-seq Samples.

567 Nuclei were isolated from frozen mouse iWAT samples as previously described, with the following
568 modifications to integrate hash multiplexing and FANS-assisted nuclear quality thresholding and
569 sample pooling (Drokhlyansky et al., 2020; Slyper et al., 2020). Briefly, 300 mg of flash-frozen
570 adipose samples were held on dry ice until immediately before nuclei isolation, and all sample
571 handling steps were performed on ice. Each sample was placed into a gentleMACS C tube
572 (Miltenyi Biotec, 130-093-237) with 2 mL freshly prepared TST buffer (0.03% Tween 20 (Bio-Rad),
573 0.01% Molecular Grade BSA (New England Biolabs), 146 mM NaCl (ThermoFisher Scientific), 1
574 mM CaCl₂ (VWR International), 21 mM MgCl₂ (Sigma Aldrich), and 10 mM Tris-HCl pH 7.5
575 (ThermoFisher Scientific) in ultrapure water (ThermoFisher Scientific)) with 0.2 U/μL of Protector
576 RNase Inhibitor (Sigma Aldrich, RNAINH-RO). gentleMACS C tubes were then placed on the
577 gentleMACS Dissociator (Miltenyi Biotec) and tissue was dissociated by running the program
578 "mr_adipose_01" three times, and then incubated on ice for 10 minutes. Lysate was passed
579 through a 40 μm nylon filter (CellTreat) and collected into a 50 mL conical tube (Corning). Filter
580 was rinsed with 3 mL of freshly prepared ST buffer (146 mM NaCl, 1 mM CaCl₂, 21 mM MgCl₂;
581 10 mM Tris-HCl pH 7.5) with 0.2 U/μL RNase Inhibitor, and collected into the same tube. Flow-
582 through was passed through a 20 μm pre-separation filter (Miltenyi Biotec) set on top of a 5 mL
583 FACS tube (Corning) and collected into the same tube. Suspension was centrifuged in a swinging-
584 bucket centrifuge (Eppendorf) at 500 × g for 5 minutes at 4°C with brake set to low. Following
585 centrifugation, supernatant was removed and 5 mL of PBS pH 7.4 (ThermoFisher Scientific) with

586 0.02% BSA and 0.2 U/ μ L RNase Inhibitor was added without resuspending the nuclear pellet.
587 Sample was centrifuged again at 500 \times g for 5 minutes at 4°C with brake set to low. Following
588 centrifugation, supernatant was removed, and the nuclear pellet was resuspended in 1 mL PBS-
589 0.02% BSA with 0.2 U/ μ L RNase Inhibitor. Each sample was split into two 500 μ L aliquots and
590 transferred to new 5 mL FACS tubes for subsequent hashing. Each aliquot of resuspended nuclei
591 was stained with NucBlue (ThermoFisher, R37605), labeled with 1 μ g of a unique TotalSeq anti-
592 Nuclear Pore Complex Proteins Hashtag Antibody (Biolegend), and then incubated on ice for 30
593 minutes. Suspension was centrifuged at 500 \times g for 5 minutes at 4°C with brake set to low.
594 Following centrifugation, 450 μ L of supernatant was removed and the nuclear pellet was
595 resuspended in 450 μ L PBS-0.02% BSA with 0.2 U/ μ L RNase Inhibitor. For nuclear quality
596 thresholding, fluorescence-activated nuclear sorting (FANS) was implemented to collect 4,000-
597 4,300 nuclei from hashtagged aliquots directly into a shared well of a 96-well PCR plate (Thermo
598 Scientific) containing 24.6 μ L of 10X RT Reagent B with 1U/ μ L RNase Inhibitor on a Beckman
599 Coulter MoFlo AstriosEQ fitted with a 70 μ m nozzle. High-quality nuclei were selected by initial
600 gating at 360 nm with laser filter 405-448/59 followed by SSC-H and FSC-H to remove doublets
601 and unlysed cells. Once all sample aliquots were FANS-sorted, the pool of 43,000 nuclei was
602 loaded on the 10x Chromium controller (10x Genomics) according to the manufacturer's protocol.
603 cDNA and gene expression libraries were generated according to the manufacturer's instructions
604 (10x Genomics). Libraries of hashtag oligo fractions were generated according to the
605 manufacturer's instructions (Biolegend). cDNA and gene expression library fragment sizes were
606 assessed with a DNA High Sensitivity Bioanalyzer Chip (Agilent). cDNA and gene expression
607 libraries were quantified using the Qubit dsDNA High Sensitivity assay kit (ThermoFisher,
608 Q32854). Gene expression libraries were multiplexed and sequenced on the Nextseq 500
609 (Illumina) using a 75-cycle kit and the following read structure: Read 1: 28 cycles, Read 2: 55
610 cycles, Index Read 1: 8 cycles.

611

612 **Bioinformatics analysis**

613 Single Cell RNA Sequencing

614 Data was processed using the Cell Ranger pipeline (10x Genomics, v.3.1.0) for demultiplexing
615 and alignment of sequencing reads to the mm10 transcriptome and creation of feature-barcode
616 matrices. The cell ranger output files were read into R (version 4.1.1) and processed utilizing the
617 standard Seurat CCA integrated workflow (version 4.3.0). Each of the six samples went through
618 a first phase of filtering, where only cells that recorded more than 200 features and only features
619 present in a minimum of 3 cells were kept. Each sample was filtered prior to downstream analysis

620 on nCount_RNA, nFeature_RNA, and mitochondrial percentages. Samples were then normalized
621 using a LogNormalization method with a scaling factor of 10000 followed by FindVariableFeatures
622 using Variance Stabilization Transformation with the top 6000 features to be returned. The
623 samples were scored on their cell cycle phases which would be used in the regression later. The
624 FindIntegrationAnchors function using the CCA reduction method and IntegrateData was utilized
625 to integrate the data together. The integrated data-set was then scaled in which mitochondrial
626 percentage and cell cycle state was regressed out. A principal component analysis was performed
627 and the top 15 dimensions were kept. Uniform Manifold and Projection (UMAP) was run on the
628 dataset, in addition to FindNeighbors and FindClusters. Differential gene expression between
629 clusters was performed using the FindMarkers function with the Wilcoxon test in Seurat. Violin plots
630 and individual UMAP plots were all generated using the Seurat toolkit VlnPlot and FeaturePlot
631 functions, respectively. Heatmaps were generated utilizing the pheatmap package (version
632 1.0.12).

633

634 Single Nucleus RNA Sequencing

635 Raw sequencing reads were demultiplexed to FASTQ format files using bcl2fastq (Illumina;
636 version 2.20.0). Digital expression matrices were generated from the FASTQ files using Cell
637 Ranger (Zheng et al., 2017)(version 6.1.2) with the option to include intronic reads (--include-
638 introns). Reads were aligned against the GRCm38 mouse genome assembly and gene counts
639 were obtained, per-droplet, by summarizing exonic and intronic UMIs that overlapped with the
640 GENCODE mouse annotation (release 24) for each gene symbol. In order to adjust for
641 downstream effects of ambient RNA expression within mouse nuclei, we used the "remove-
642 background" module from CellBender (Fleming et al., 2022) (version 0.2.0) to remove counts due
643 to ambient RNA molecules from the count matrices and to estimate the true cells. Genes were
644 subsequently filtered such that only genes detected in two or more cells and with at least 6 total
645 counts (across all cells) were retained. Sample demultiplexing via hashtag oligonucleotide
646 sequences (HTOs) was performed with the Cumulus sc/snRNA-Seq processing pipeline (Li et al.,
647 2020). Specifically, HTO quantification was performed with the [Cumulus Tool on Feature
648 Barcoding](#), which provided a cell-by-HTO count matrix. This HTO count matrix, along with the
649 gene count matrices generated via Cell Ranger (above) were used to assign each cell to their
650 respective sample(s) with the demuxEM program. Only cells that were identified as singlets were
651 retained (i.e. no cells identified as a multiplet or unassignable) in the per-sample CellBender-ed
652 gene count matrices.

653 Cellbender output files were read into R (version 4.1.1) and processed utilizing the
654 standard Seurat CCA and later RPCA integration workflows (version 4.3.0). Each of the hashed
655 samples (24 in total) were merged with their respective pair to have a total of twelve samples
656 consisting of six different groups. Each sample was filtered prior to downstream analysis based
657 on their nCount_RNA, nFeature_RNA, and mitochondrial percentages. Samples were then
658 normalized using a LogNormalization method with a scaling factor of 10000 followed by
659 FindVariableFeatures using a Variance-Stabilizing Transformation as the method with the top
660 2000 features to be returned. The FindIntegrationAnchors function using the CCA reduction
661 method and IntegrateData was utilized to integrate the data together. The integrated data-set was
662 then scaled on which mitochondrial percentage was regressed. A principal component analysis
663 was performed in which only the top 18 dimensions were retained. Uniform Manifold and
664 Projection (UMAP), FindNeighbors, and FindClusters with a resolution of 0.4 was performed on
665 the dataset. To remove doublets in the dataset, we used the package scDbfFinder (1.8.0) and
666 their function scDbfFinder with the parameters of samples set to our twelve samples, dbr set to
667 NULL, dbr.sd set to 1, clusters set to FALSE, and multiSampleMode set to split. The object was
668 then subsetted to only contain expected singlets. Differential gene expression between clusters
669 was performed using the FindMarkers function with the Wilcoxon test in Seurat. Violin plots and
670 individual UMAP plots were all generated using the Seurat toolkit VlnPlot and FeaturePlot
671 functions, respectively. Heatmaps were generated utilizing the dittoSeq package (1.9.1) and
672 pheatmap package (version 1.0.12).

673 After identifying the adipocyte population, we subsetted our object on that population,
674 extracting the raw RNA counts on the cells for each of the six samples (YTN, OTN, Y3D, O3D,
675 Y14D, O14D) (Y is young, O is "Old" or as referred to in this paper, Aged). These samples were
676 then integrated together using the standard RPCA integration workflow. There was no further
677 filtering done on the reintegrated adipocyte population. Samples were normalized using a
678 LogNormalization method with a scaling factor of 10000 followed by FindvariableFeatures using
679 a Variance-Stabilizing Transformation as the method with the top 2000 features to be returned.
680 The function SelectIntegrationFeatures was performed on the dataset where it was then scaled
681 on which mitochondrial percentage was regressed, and principal components were found using
682 the ScaleData and RunPCA functions. The FindIntegrationAnchors function using the ROCA
683 reduction method and a k.anchors of 20 and IntegrateData was utilized to integrate the data
684 together. After integration, the dataset was then scaled in which mitochondrial percentage was
685 regressed on again. A principal component analysis was performed in which only the top 18
686 dimensions were retained. Uniform Manifold and Projection (UMAP), FindNeighbors, and

687 FindClusters with a resolution of 0.2 was performed on the dataset. Differential gene expression
688 between clusters was performed using the FindMarkers function with a Wilcoxon signed-rank test
689 as the method in Seurat. Violin plots and individual UMAP plots were all generated using the
690 Seurat toolkit VlnPlot and FeaturePlot functions, respectively. Heatmaps were generated utilizing
691 the dittoSeq package (1.9.1) and pheatmap package (version 1.0.12).

692 Enrichment analysis was performed on the positively expressed genes with a \log_2 fold
693 change (LFC) > 0.25 and a P_{adjusted} value < 0.01 on comparison of the young 14 days cold and
694 old 14 days cold groups in the DNL high cluster. The generated gene list, which was in order of
695 significance, was fed into g:Profiler (version 0.2.1) using default parameters except with
696 modifications to query as an ordered query against the 'mmusculus' database, a gSCS correction
697 method for multiple testing, with domain scope set to annotated, and sources set to the Reactome
698 database. The top six enriched pathways yielded from the database were taken and displayed in
699 order of P_{adjusted} value.

700

701 **Statistical methods**

702 All bar graphs represent the mean \pm SE. A Student's t-test was used when 2 groups were
703 compared. Where multiple conditions were compared, we applied a Holm-Šidák correction for
704 multiple comparisons. p values are indicated by asterisks and defined as *p < 0.05 , **p < 0.01
705 and ***p < 0.001 . All statistics were calculated with GraphPad Prism Version 9.5.0.

706

707 **References**

- 708 Amiya Kumar Ghosh, M. O. B., Theresa Mau, Nathan Qi, and Raymond Yung. (2019). Adipose
709 Tissue Senescence and Inflammation in Aging is Reversed by the Young Milieu. *J*
710 *Gerontol A Biol Sci Med Sci*, 74(11), 1709-1715. doi:10.1093/gerona/gly290
- 711 Barreau, C., Labit, E., Guissard, C., Rouquette, J., Boizeau, M. L., Gani Koumassi, S., . . .
712 Lorsignol, A. (2016). Regionalization of browning revealed by whole subcutaneous
713 adipose tissue imaging. *Obesity (Silver Spring)*, 24(5), 1081-1089. doi:10.1002/oby.21455
- 714 Becher, T., Palanisamy, S., Kramer, D. J., Eljalby, M., Marx, S. J., Wibmer, A. G., . . . Cohen, P.
715 (2021). Brown adipose tissue is associated with cardiometabolic health. *Nat Med*, 27(1),
716 58-65. doi:10.1038/s41591-020-1126-7
- 717 Berry, D. C., Jiang, Y., Arpke, R. W., Close, E. L., Uchida, A., Reading, D., . . . Graff, J. M.
718 (2017). Cellular Aging Contributes to Failure of Cold-Induced Beige Adipocyte Formation
719 in Old Mice and Humans. *Cell Metab*, 25(1), 166-181. doi:10.1016/j.cmet.2016.10.023
- 720 Berry, D. C., Jiang, Y., & Graff, J. M. (2016). Mouse strains to study cold-inducible beige
721 progenitors and beige adipocyte formation and function. *Nat Commun*, 7, 10184.
722 doi:10.1038/ncomms10184
- 723 Bordicchia, M., Liu, D., Amri, E. Z., Ailhaud, G., Dessi-Fulgheri, P., Zhang, C., . . . Collins, S.
724 (2012). Cardiac natriuretic peptides act via p38 MAPK to induce the brown fat thermogenic

- 725 program in mouse and human adipocytes. *J Clin Invest*, 122(3), 1022-1036.
726 doi:10.1172/JCI59701
- 727 Brosseau, C., Colas, L., Magnan, A., & Brouard, S. (2018). CD9 Tetraspanin: A New Pathway for
728 the Regulation of Inflammation? *Front Immunol*, 9, 2316. doi:10.3389/fimmu.2018.02316
- 729 Burl, R. B., Ramseyer, V. D., Rondini, E. A., Pique-Regi, R., Lee, Y. H., & Granneman, J. G.
730 (2018). Deconstructing Adipogenesis Induced by beta3-Adrenergic Receptor Activation
731 with Single-Cell Expression Profiling. *Cell Metab*, 28(2), 300-309 e304.
732 doi:10.1016/j.cmet.2018.05.025
- 733 Cannon, B., & Nedergaard, J. (2004). Brown Adipose Tissue: Function and Physiological
734 Significance. *Physiology Review*, 84, 277–359. doi:10.1152/physrev.00015.2003
- 735 Cederberg, A., Gronning, L. M., Ahren, B., Tasken, K., Carlsson, P., & Enerback, S. (2001).
736 FOXC2 is a winged helix gene that counteracts obesity, hypertriglyceridemia, and diet-
737 induced insulin resistance. *Cell*, 106(5), 563-573. doi:10.1016/s0092-8674(01)00474-3
- 738 Chi, J., Wu, Z., Choi, C. H. J., Nguyen, L., Teegene, S., Ackerman, S. E., . . . Cohen, P. (2018).
739 Three-Dimensional Adipose Tissue Imaging Reveals Regional Variation in Beige Fat
740 Biogenesis and PRDM16-Dependent Sympathetic Neurite Density. *Cell Metab*, 27(1),
741 226-236 e223. doi:10.1016/j.cmet.2017.12.011
- 742 Chouchani, E. T., Kazak, L., & Spiegelman, B. M. (2019). New Advances in Adaptive
743 Thermogenesis: UCP1 and Beyond. *Cell Metab*, 29(1), 27-37.
744 doi:10.1016/j.cmet.2018.11.002
- 745 Chung, M. I., Bujnis, M., Barkauskas, C. E., Kobayashi, Y., & Hogan, B. L. M. (2018). Niche-
746 mediated BMP/SMAD signaling regulates lung alveolar stem cell proliferation and
747 differentiation. *Development*, 145(9). doi:10.1242/dev.163014
- 748 Cohen, P., Levy, J. D., Zhang, Y., Frontini, A., Kolodin, D. P., Svensson, K. J., . . . Spiegelman,
749 B. M. (2014). Ablation of PRDM16 and beige adipose causes metabolic dysfunction and a
750 subcutaneous to visceral fat switch. *Cell*, 156(1-2), 304-316.
751 doi:10.1016/j.cell.2013.12.021
- 752 Coue, M., Barquissau, V., Morigny, P., Louche, K., Lefort, C., Mairal, A., . . . Moro, C. (2018).
753 Natriuretic peptides promote glucose uptake in a cGMP-dependent manner in human
754 adipocytes. *Sci Rep*, 8(1), 1097. doi:10.1038/s41598-018-19619-0
- 755 Cypess, A. M., Chen, Y. C., Sze, C., Wang, K., English, J., Chan, O., . . . Kahn, C. R. (2012). Cold
756 but not sympathomimetics activates human brown adipose tissue in vivo. *Proc Natl Acad
757 Sci U S A*, 109(25), 10001-10005. doi:10.1073/pnas.1207911109
- 758 Cypess, A. M., Lehman, S., Williams, G., Tal, I., Rodman, D., Goldfine, A. B., . . . Kahn, C. R.
759 (2009). Identification and importance of brown adipose tissue in adult humans. *N Engl J
760 Med*, 360(15), 1509-1517. doi:10.1056/NEJMoa0810780
- 761 Dichamp, J., Barreau, C., Guissard, C., Carriere, A., Martinez, Y., Descombes, X., . . . Lorsignol,
762 A. (2019). 3D analysis of the whole subcutaneous adipose tissue reveals a complex spatial
763 network of interconnected lobules with heterogeneous browning ability. *Sci Rep*, 9(1),
764 6684. doi:10.1038/s41598-019-43130-9
- 765 Drokhlyansky, E., Smillie, C. S., Van Wittenberghe, N., Ericsson, M., Griffin, G. K., Eraslan, G.,
766 . . . Regev, A. (2020). The Human and Mouse Enteric Nervous System at Single-Cell
767 Resolution. *Cell*, 182(6), 1606-1622 e1623. doi:10.1016/j.cell.2020.08.003
- 768 Ferrero, R., Rainer, P., & Deplancke, B. (2020). Toward a Consensus View of Mammalian
769 Adipocyte Stem and Progenitor Cell Heterogeneity. *Trends Cell Biol*, 30(12), 937-950.
770 doi:10.1016/j.tcb.2020.09.007

- 771 Fleming, S. J., Chaffin, M. D., Arduini, A., Akkad, A.-D., Banks, E., Marioni, J. C., . . . Babadi,
772 M. (2022). CellBender remove-background: a deep generative model for unsupervised
773 removal of background noise from scRNA-seq datasets. *bioRxiv*. doi:10.1101/791699
- 774 Gentili, A., Frangione, M. R., Albini, E., Vacca, C., Ricci, M. A., De Vuono, S., . . . Orabona, C.
775 (2017). Modulation of natriuretic peptide receptors in human adipose tissue: molecular
776 mechanisms behind the "natriuretic handicap" in morbidly obese patients. *Transl Res*, *186*,
777 52-61. doi:10.1016/j.trsl.2017.06.001
- 778 Goncalves, L. F., Machado, T. Q., Castro-Pinheiro, C., de Souza, N. G., Oliveira, K. J., &
779 Fernandes-Santos, C. (2017). Ageing is associated with brown adipose tissue remodelling
780 and loss of white fat browning in female C57BL/6 mice. *Int J Exp Pathol*, *98*(2), 100-108.
781 doi:10.1111/iep.12228
- 782 Graja, A., Garcia-Carrizo, F., Jank, A. M., Gohlke, S., Ambrosi, T. H., Jonas, W., . . . Schulz, T.
783 J. (2018). Loss of periostin occurs in aging adipose tissue of mice and its genetic ablation
784 impairs adipose tissue lipid metabolism. *Aging Cell*, *17*(5), e12810.
785 doi:10.1111/accel.12810
- 786 Jaitin, D. A., Adlung, L., Thaïss, C. A., Weiner, A., Li, B., Descamps, H., . . . Amit, I. (2019).
787 Lipid-Associated Macrophages Control Metabolic Homeostasis in a Trem2-Dependent
788 Manner. *Cell*, *178*(3), 686-698 e614. doi:10.1016/j.cell.2019.05.054
- 789 Jespersen, N. Z., Larsen, T. J., Peijs, L., Daugaard, S., Homoe, P., Loft, A., . . . Scheele, C. (2013).
790 A classical brown adipose tissue mRNA signature partly overlaps with brite in the
791 supraclavicular region of adult humans. *Cell Metab*, *17*(5), 798-805.
792 doi:10.1016/j.cmet.2013.04.011
- 793 Kovacova, Z., Tharp, W. G., Liu, D., Wei, W., Xie, H., Collins, S., & Pratley, R. E. (2016).
794 Adipose tissue natriuretic peptide receptor expression is related to insulin sensitivity in
795 obesity and diabetes. *Obesity (Silver Spring)*, *24*(4), 820-828. doi:10.1002/oby.21418
- 796 Lee, Y. H., Kim, S. N., Kwon, H. J., & Granneman, J. G. (2017). Metabolic heterogeneity of
797 activated beige/brite adipocytes in inguinal adipose tissue. *Sci Rep*, *7*, 39794.
798 doi:10.1038/srep39794
- 799 Li, B., Gould, J., Yang, Y., Sarkizova, S., Tabaka, M., Ashenberg, O., . . . Regev, A. (2020).
800 Cumulus provides cloud-based data analysis for large-scale single-cell and single-nucleus
801 RNA-seq. *Nat Methods*, *17*(8), 793-798. doi:10.1038/s41592-020-0905-x
- 802 Long, J. Z., Svensson, K. J., Tsai, L., Zeng, X., Roh, H. C., Kong, X., . . . Spiegelman, B. M.
803 (2014). A smooth muscle-like origin for beige adipocytes. *Cell Metab*, *19*(5), 810-820.
804 doi:10.1016/j.cmet.2014.03.025
- 805 Marcelin, G., Ferreira, A., Liu, Y., Atlan, M., Aron-Wisnewsky, J., Pelloux, V., . . . Clement, K.
806 (2017). A PDGFRalpha-Mediated Switch toward CD9(high) Adipocyte Progenitors
807 Controls Obesity-Induced Adipose Tissue Fibrosis. *Cell Metab*, *25*(3), 673-685.
808 doi:10.1016/j.cmet.2017.01.010
- 809 Martinez Calejman, C., Trefely, S., Entwisle, S. W., Luciano, A., Jung, S. M., Hsiao, W., . . .
810 Guertin, D. A. (2020). mTORC2-AKT signaling to ATP-citrate lyase drives brown
811 adipogenesis and de novo lipogenesis. *Nat Commun*, *11*(1), 575. doi:10.1038/s41467-020-
812 14430-w
- 813 McDonald, M. E., Li, C., Bian, H., Smith, B. D., Layne, M. D., & Farmer, S. R. (2015). Myocardin-
814 related transcription factor A regulates conversion of progenitors to beige adipocytes. *Cell*,
815 *160*(1-2), 105-118. doi:10.1016/j.cell.2014.12.005

- 816 Merrick, D., Sakers, A., Irgebay, Z., Okada, C., Calvert, C., Morley, M. P., . . . Seale, P. (2019).
817 Identification of a mesenchymal progenitor cell hierarchy in adipose tissue. *Science*,
818 364(6438). doi:10.1126/science.aav2501
- 819 Moro, C., Galitzky, J., Sengenès, C., Crampes, F., Lafontan, M., & Berlan, M. (2004). Functional
820 and pharmacological characterization of the natriuretic peptide-dependent lipolytic
821 pathway in human fat cells. *J Pharmacol Exp Ther*, 308(3), 984-992.
822 doi:10.1124/jpet.103.060913
- 823 Mottillo, E. P., Balasubramanian, P., Lee, Y. H., Weng, C., Kershaw, E. E., & Granneman, J. G.
824 (2014). Coupling of lipolysis and de novo lipogenesis in brown, beige, and white adipose
825 tissues during chronic beta3-adrenergic receptor activation. *J Lipid Res*, 55(11), 2276-
826 2286. doi:10.1194/jlr.M050005
- 827 Nguyen, H. P., Lin, F., Yi, D., Xie, Y., Dinh, J., Xue, P., & Sul, H. S. (2021). Aging-dependent
828 regulatory cells emerge in subcutaneous fat to inhibit adipogenesis. *Dev Cell*, 56(10), 1437-
829 1451 e1433. doi:10.1016/j.devcel.2021.03.026
- 830 Pfannenberger, C., Werner, M. K., Ripkens, S., Stef, I., Deckert, A., Schmadl, M., . . . Stefan, N.
831 (2010). Impact of age on the relationships of brown adipose tissue with sex and adiposity
832 in humans. *Diabetes*, 59(7), 1789-1793. doi:10.2337/db10-0004
- 833 Prabata, A., Ikeda, K., Rahardini, E. P., Hirata, K. I., & Emoto, N. (2021). GPNMB plays a
834 protective role against obesity-related metabolic disorders by reducing macrophage
835 inflammatory capacity. *J Biol Chem*, 297(5), 101232. doi:10.1016/j.jbc.2021.101232
- 836 Rogers, N. H., Landa, A., Park, S., & Smith, R. G. (2012). Aging leads to a programmed loss of
837 brown adipocytes in murine subcutaneous white adipose tissue. *Aging Cell*, 11(6), 1074-
838 1083. doi:10.1111/accel.12010
- 839 Rosell, M., Kaforou, M., Frontini, A., Okolo, A., Chan, Y. W., Nikolopoulou, E., . . . Christian,
840 M. (2014). Brown and white adipose tissues: intrinsic differences in gene expression and
841 response to cold exposure in mice. *Am J Physiol Endocrinol Metab*, 306(8), E945-964.
842 doi:10.1152/ajpendo.00473.2013
- 843 Rosenwald, M., Perdikari, A., Rulicke, T., & Wolfrum, C. (2013). Bi-directional interconversion
844 of brite and white adipocytes. *Nat Cell Biol*, 15(6), 659-667. doi:10.1038/ncb2740
- 845 Saade, M., Araujo de Souza, G., Scavone, C., & Kinoshita, P. F. (2021). The Role of GPNMB in
846 Inflammation. *Front Immunol*, 12, 674739. doi:10.3389/fimmu.2021.674739
- 847 Saito, M., Okamatsu-Ogura, Y., Matsushita, M., Watanabe, K., Yoneshiro, T., Nio-Kobayashi, J.,
848 . . . Tsujisaki, M. (2009). High incidence of metabolically active brown adipose tissue in
849 healthy adult humans: effects of cold exposure and adiposity. *Diabetes*, 58(7), 1526-1531.
850 doi:10.2337/db09-0530
- 851 Sakers, A., De Siqueira, M. K., Seale, P., & Villanueva, C. J. (2022). Adipose-tissue plasticity in
852 health and disease. *Cell*, 185(3), 419-446. doi:10.1016/j.cell.2021.12.016
- 853 Sanchez-Gurmaches, J., Tang, Y., Jespersen, N. Z., Wallace, M., Martinez Calejman, C., Gujja,
854 S., . . . Guertin, D. A. (2018). Brown Fat AKT2 Is a Cold-Induced Kinase that Stimulates
855 ChREBP-Mediated De Novo Lipogenesis to Optimize Fuel Storage and Thermogenesis.
856 *Cell Metab*, 27(1), 195-209 e196. doi:10.1016/j.cmet.2017.10.008
- 857 Seale, P., Conroe, H. M., Estall, J., Kajimura, S., Frontini, A., Ishibashi, J., . . . Spiegelman, B. M.
858 (2011). Prdm16 determines the thermogenic program of subcutaneous white adipose tissue
859 in mice. *J Clin Invest*, 121(1), 96-105. doi:10.1172/JCI44271

- 860 Sengenès, C., Berlan, M., Glisezinski, I., Lafontan, M., & Galitzky, J. (2000). Natriuretic peptides:
861 a new lipolytic pathway in human adipocytes. *The FASEB Journal*, *14*(10), 1345-1351.
862 doi:10.1096/fasebj.14.10.1345
- 863 Sengenès, C., Bouloumie, A., Hauner, H., Berlan, M., Busse, R., Lafontan, M., & Galitzky, J.
864 (2003). Involvement of a cGMP-dependent pathway in the natriuretic peptide-mediated
865 hormone-sensitive lipase phosphorylation in human adipocytes. *J Biol Chem*, *278*(49),
866 48617-48626. doi:10.1074/jbc.M303713200
- 867 Shamsi, F., Piper, M., Ho, L. L., Huang, T. L., Gupta, A., Streets, A., . . . Tseng, Y. H. (2021).
868 Vascular smooth muscle-derived Trpv1(+) progenitors are a source of cold-induced
869 thermogenic adipocytes. *Nat Metab*, *3*(4), 485-495. doi:10.1038/s42255-021-00373-z
- 870 Shao, M., Ishibashi, J., Kusminski, C. M., Wang, Q. A., Hepler, C., Vishvanath, L., . . . Gupta, R.
871 K. (2016). Zfp423 Maintains White Adipocyte Identity through Suppression of the Beige
872 Cell Thermogenic Gene Program. *Cell Metab*, *23*(6), 1167-1184.
873 doi:10.1016/j.cmet.2016.04.023
- 874 Shao, M., Wang, Q. A., Song, A., Vishvanath, L., Busbuso, N. C., Scherer, P. E., & Gupta, R. K.
875 (2019). Cellular Origins of Beige Fat Cells Revisited. *Diabetes*, *68*(10), 1874-1885.
876 doi:10.2337/db19-0308
- 877 Slyper, M., Porter, C. B. M., Ashenberg, O., Waldman, J., Drokhlyansky, E., Wakiro, I., . . . Regev,
878 A. (2020). A single-cell and single-nucleus RNA-Seq toolbox for fresh and frozen human
879 tumors. *Nat Med*, *26*(5), 792-802. doi:10.1038/s41591-020-0844-1
- 880 St-Onge, M.-P. (2005). Relationship between body composition changes and changes in physical
881 function and metabolic risk factors in aging. *Current Opinion in Clinical Nutrition and*
882 *Metabolic Care*, *8*, 523-528.
- 883 Stine, R. R., Shapira, S. N., Lim, H. W., Ishibashi, J., Harms, M., Won, K. J., & Seale, P. (2016).
884 EBF2 promotes the recruitment of beige adipocytes in white adipose tissue. *Mol Metab*,
885 *5*(1), 57-65. doi:10.1016/j.molmet.2015.11.001
- 886 Ussar, S., Lee, K. Y., Dankel, S. N., Boucher, J., Haering, M. F., Kleinridders, A., . . . Kahn, C. R.
887 (2014). ASC-1, PAT2, and P2RX5 are cell surface markers for white, beige, and brown
888 adipocytes. *Sci Transl Med*, *6*(247), 247ra103. doi:10.1126/scitranslmed.3008490
- 889 Wang, Q. A., Tao, C., Gupta, R. K., & Scherer, P. E. (2013). Tracking adipogenesis during white
890 adipose tissue development, expansion and regeneration. *Nat Med*, *19*(10), 1338-1344.
891 doi:10.1038/nm.3324
- 892 Wang, W., Ishibashi, J., Trefely, S., Shao, M., Cowan, A. J., Sakers, A., . . . Seale, P. (2019). A
893 PRDM16-Driven Metabolic Signal from Adipocytes Regulates Precursor Cell Fate. *Cell*
894 *Metab*, *30*(1), 174-189 e175. doi:10.1016/j.cmet.2019.05.005
- 895 Wang, W., & Seale, P. (2016). Control of brown and beige fat development. *Nat Rev Mol Cell*
896 *Biol*, *17*(11), 691-702. doi:10.1038/nrm.2016.96
- 897 Wu, J., Bostrom, P., Sparks, L. M., Ye, L., Choi, J. H., Giang, A. H., . . . Spiegelman, B. M. (2012).
898 Beige adipocytes are a distinct type of thermogenic fat cell in mouse and human. *Cell*,
899 *150*(2), 366-376. doi:10.1016/j.cell.2012.05.016
- 900 Yoneshiro, T., Aita, S., Matsushita, M., Okamatsu-Ogura, Y., Kameya, T., Kawai, Y., . . . Saito,
901 M. (2011). Age-related decrease in cold-activated brown adipose tissue and accumulation
902 of body fat in healthy humans. *Obesity (Silver Spring)*, *19*(9), 1755-1760.
903 doi:10.1038/oby.2011.125
- 904 Yu, X. X., Lewin, D. A., Forrest, W., & Adams, S. H. (2002). Cold elicits the simultaneous
905 induction of fatty acid synthesis and beta-oxidation in murine brown adipose tissue:

906 prediction from differential gene expression and confirmation in vivo. *FASEB J*, 16(2),
907 155-168. doi:10.1096/fj.01-0568com
908 Zheng, G. X., Terry, J. M., Belgrader, P., Ryvkin, P., Bent, Z. W., Wilson, R., . . . Bielas, J. H.
909 (2017). Massively parallel digital transcriptional profiling of single cells. *Nat Commun*, 8,
910 14049. doi:10.1038/ncomms14049
911